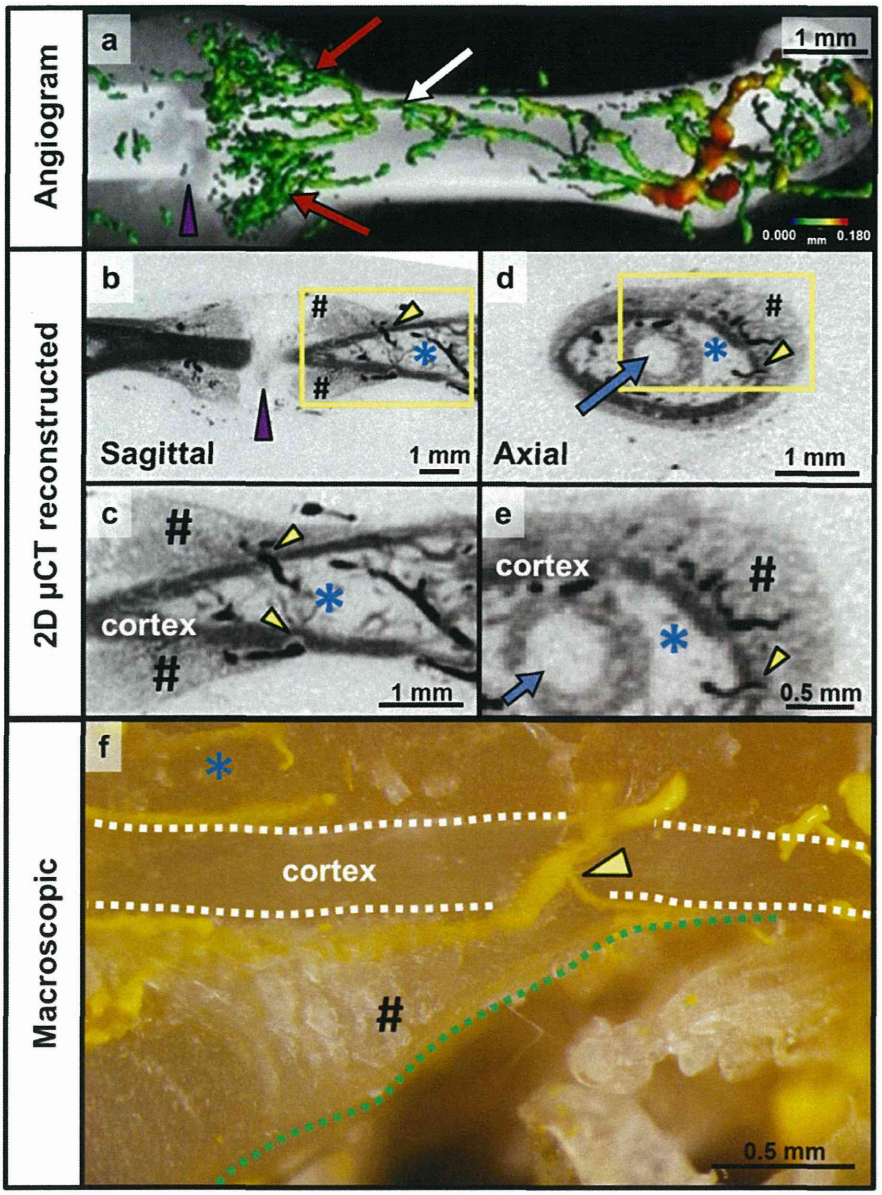

Fig. 4. Newly formed vasculature arising from intact intramedullary vasculature adjacent to healing fracture (a) 10 days post fracture, small contrast-filled blood vessels in the extramedullary fracture callus and endosteal areas of the intramedullary cavity (red arrow) appear to arise from intact intramedullary vessels (white arrow) proximal to the fracture callus (purple arrowhead indicates fracture site). (b–e) Two dimensional reconstructed sagittal (b, c) and axial (d, e) µCT images illustrate multiple anastomoses (yellow arrowheads) between the intramedullary (blue asterisks) and extramedullary (#) vasculature (c and e are magnified regions highlighted in b and d, respectively). The purple arrowhead indicates the fracture site (b). The site of the 23-G fixation pin in the axial image is denoted with a blue arrow (d). Notably, the fixation pin does not occupy the entire intramedullary canal. Macroscopic dissection of the proximal end of the fracture callus (f) reveals the presence of yellow contrast-filled vessels (yellow arrowhead transgressing the cortical bone (dashed white lines) and communicating between intramedullary space (blue asterisks) and the extramedullary/subperiosteal hard callus (#, outlined by green dashed line)). Scale bars are given within the figure. Vessel diameter demarcated by color (0 and 0.18 mm) in all figures.

fracture callus (Figs. 5a, b) in contrast to the observed avascular fracture callus 7-DPF (data not shown). Histological examination shows a predominance of vascularity at the leading edge of the invading hard tissue callus in the transition zone between the hard and soft tissue calluses as wells as throughout the hard tissue callus. In agreement with macroscopic dissections and 2D-µCT reconstructions, no vessels were found within the avascular cartilaginous soft tissue callus (Fig. 5c). These findings were also observed 14-DPF however the soft tissue callus was greatly diminished in size while the hard tissue callus was much more predominate (data not shown).

Spatial patterns of vascular endothelial growth factor and its type 1 and 2 receptors during fracture healing

Vascular endothelial growth factor-A (VEGF-A) and vascular endothelial growth factor receptor 1 (VEGFR1) and 2 (VEGFR2) expressions were investigated by immunofluorescence microscopy at distinct foci along the periosteal surface 10-DPF (Figs. 6a–b). Compared to unreactive normal periosteum, the immunoreactivity of VEGF-A staining was markedly increased along the periosteum at its junction with uninvolved cortical bone, which was also the site of initial intramembranous ossification

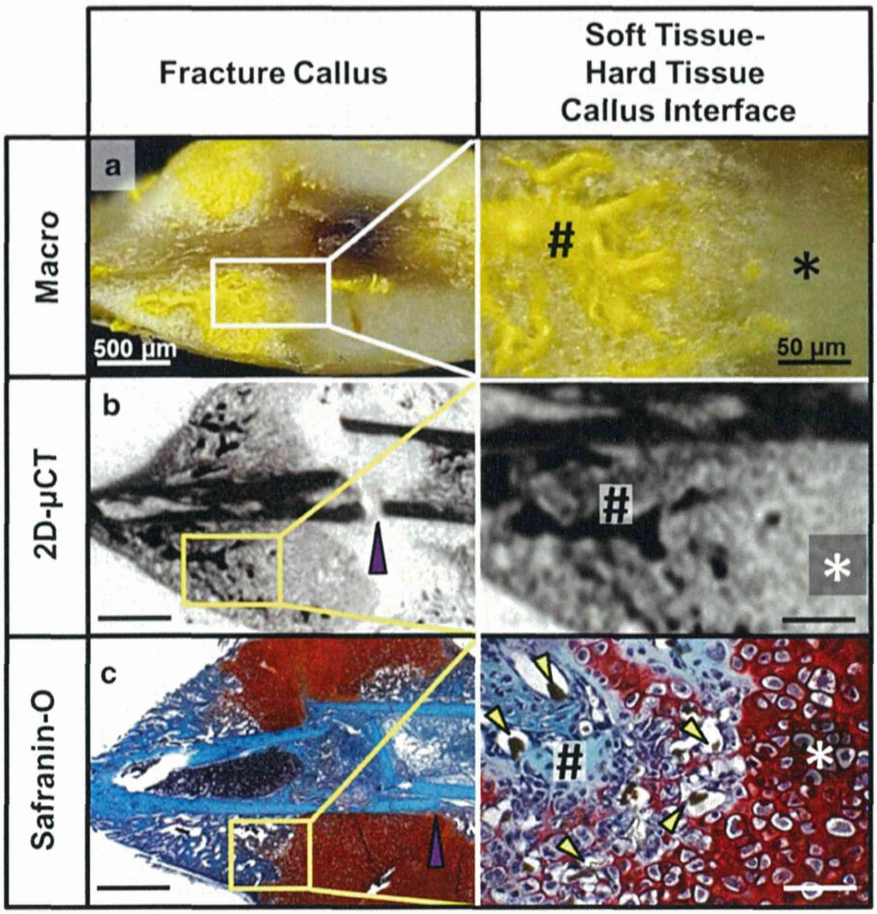

Fig. 5. Vascular polarity in hard and soft tissue fracture calluses 10 days post fracture. (a) Macroscopic dissection and (b) 2D μCT images from Microfil-injected fracture callus both demonstrate contrast agent within the extramedullary hard tissue callus, but not in soft tissue callus (see paired Safranin-O stained sections in c for comparison). At higher power magnification, a richly vascularized area with sprouting vessels (#) is seen adjacent to the avascular soft tissue callus (asterisk). (c) Paired sections of fracture callus stained with Safranin-O confirm the locations of the hard tissue callus (stained blue/green) and soft tissue callus (stained red). A higher power microscopic view of the interface between the hard tissue callus (#) and the soft tissue callus (asterisk) shows nondescript mesenchymal cells and Microfil-filled small capillaries (yellow arrowheads) replacing areas of soft callus at the interface of the hard tissue and soft tissue calluses. Scale bars: 500 μm (left) and 50 μm (right). Images are representative sections from 5 animals 10 days after fracture.

during formation of the hard tissue callus (Fig. 6c, boxes 1 & 4). These areas align anatomically with the sites at which the intramedullary vasculature is disrupted (compare with Fig. 3). In contrast, an increase in immunoreactivity of VEGF-A staining was not observed in the periosteum overlying the soft tissue callus and disrupted intramedullary vasculature in the central region of fracture callus (Fig. 6c, boxes 2 & 3).

Evaluations of multiple anatomic locations representing distinct biological activities during fracture healing demonstrate the coordinated spatial expression of VEGFA, VEGFR1 and VEGFR2 in the subperiosteal and extramedullary fracture callus 10-DPF (Figs. 7 & 8a). VEGFR1 & 2-positive cells are seen only in areas of intramembranous ossification or in hard tissue callus along the interface with soft tissue callus. These VEGFR1 & 2-positive non-chondrocytic cells are in close proximity to VEGF-A sources, either the periosteum at the proximal and distal aspects of the fracture callus or at the interface with soft tissue callus (Figs. 7 & 8b, box 1). Additionally, we observed that immature chondrocytes located deep in the soft tissue callus, and superficial to vascular deficient intramedullary bone did not express either VEGF-A, VEGFR1 or VEGFR2 (Figs. 7 & 8b, box 2). However, neighboring hypertrophic chondrocytes as well as chondrocytes situated at the transition between soft tissue and hard tissue callus expressed VEGF-A but not VEGFR1 or 2 (Figs. 7 & 8b, box 3). Juxtaposed to hypertrophic chondrocytes in the zone of transition, nondescript mesenchymal cells of the hard tissue callus invading the soft tissue callus were found to demonstrate immunoreactivity for VEGF-A, VEGFR1 and VEGFR2, demonstrating the dichotomous nature of the VEGFR-positive vascularized hard tissue callus from the avascular VEGFR1 & VEGFR2-negative soft tissue callus (Figs. 7 & 8b, box 4).

Discussion

The indispensable role of angiogenesis in fracture repair has been recognized for over a century [14,25,26]. However, elements of the temporal and spatial patterns of fracture revascularization have remained elusive. Employing a high-throughout, cost-efficient model of a displaced/stabilized fracture model with advanced imaging techniques; our data clearly supports the unifying theory of revascularization of a displaced fracture requiring both intramedullary and periosteal angiogenesis. These findings provide essential data needed to expand upon the current model of fracture revascularization developed by the pioneers of this field during the early to mid-20th century (graphical abstract, Fig. 9).

A critical aspect of fracture revascularization unanswered by the classical reports in this field was the association of intramedullary and periosteal angiogenesis. As stated above, it was thought that angiogenesis occurred in these anatomically distinct compartments independently. Trueta and Rhinelander demonstrated that angiogenesis initiated in the

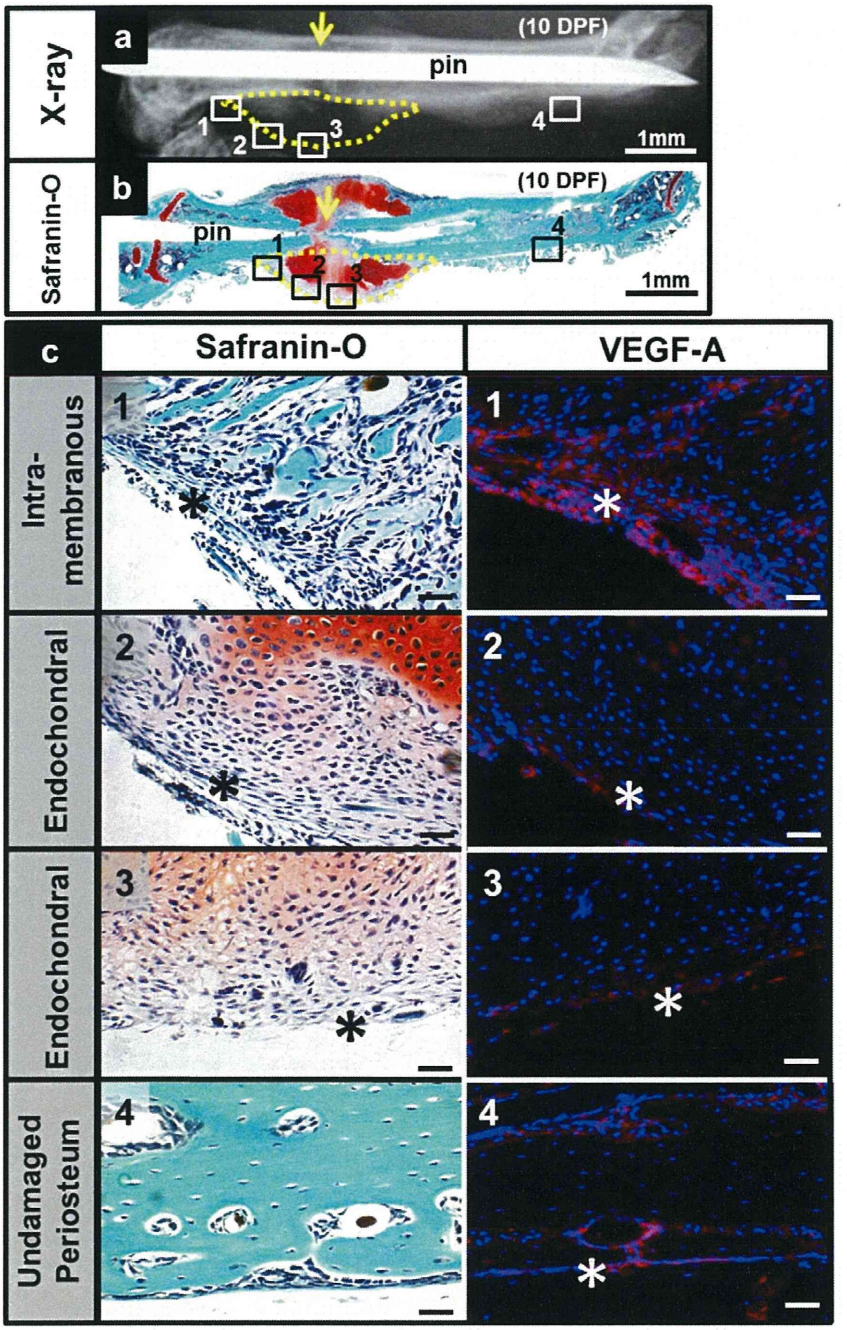

Fig. 6. VEGF-A is primarily expressed in periosteum overlying intramembranous bone formation in hard tissue callus. (a, b) Radiograph and Safranin-O-stained section of a 10 days post fracture (10-DPF) transverse femur fracture and its fracture callus (yellow dashed line). VEGF-A staining was examined at various microanatomic periosteal sites, such as the area of initial intramembranous ossification (box 1), areas overlying the soft chondroid callus (boxes 2 and 3), and an area of unreactive normal periosteum (box 4). (c) Immunofluorescence demonstrates increased immunoreactivity of VEGF-A (red) in the periosteum (asterisk) overlying the area of hard callus formation (box 1) compared to minimal levels of immunoreactivity seen in the periosteum overlying the soft callus (boxes 2 and 3) and normal unreactive periosteum on intact cortical bone (box 4). Scale bars: 40 μm.

intramedullary space directly from the remaining intact vasculature [28,30,31]. Less was known regarding the originating source of the periosteal vasculature and was conventionally believed to originate from the surrounding musculature as succinctly summarized by Kelly [31] in 1968:

> ... if the fracture is produced violently or is stabilized by intramedullary fixation, the needed new vessels originate outside the bone and the muscle vessels supply the periosteal system with these necessary new vessels.

To the contrary, our results suggest that intramedullary and periosteal angiogenesis occur in tandem, not independently. In support of this conclusion, our model is the first to demonstrate a reproducible disruption of the diaphyseal intramedullary vasculature following a fracture and or intramedullary nailing. We further show that the anatomic site of intramedullary vascular disruption corresponds to the region of initial periosteal/subperiosteal intramembranous ossification and revascularization. In 1960, Brookes showed that blood flows in a centrifugal manner from intramedullary vessels to the periosteal

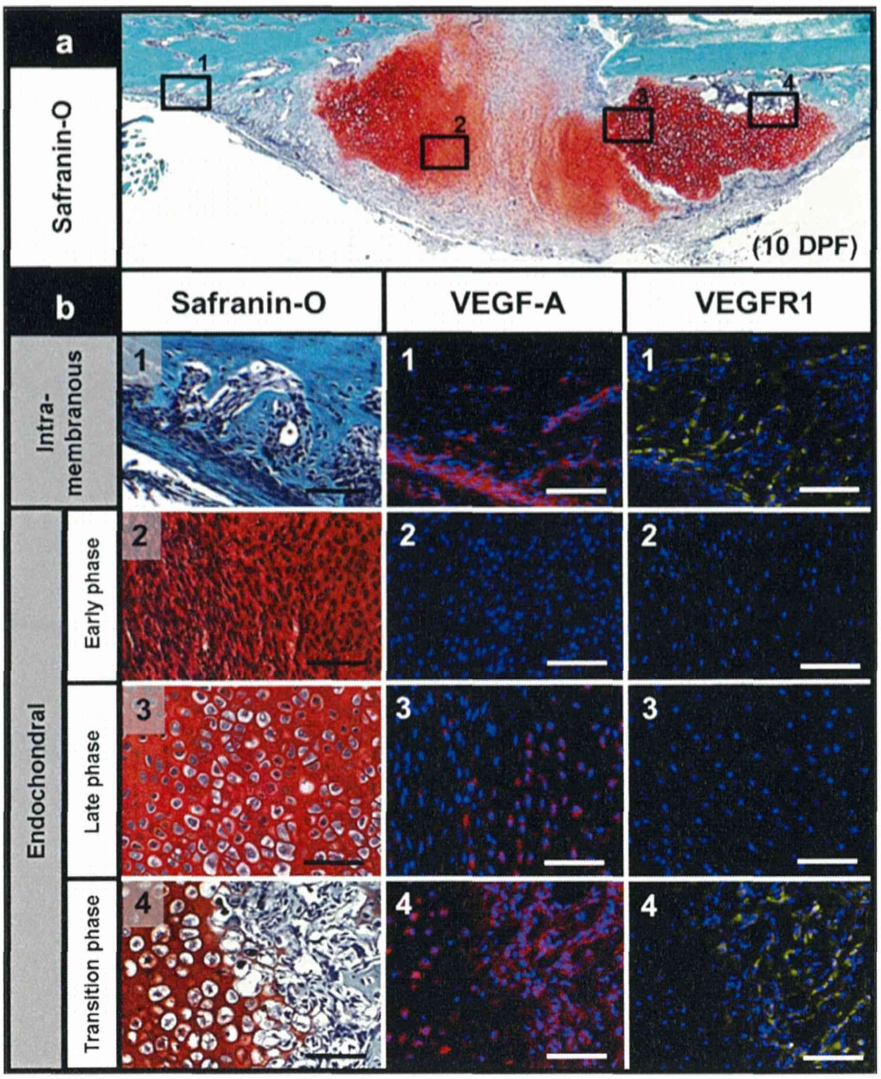

Fig. 7. Differential expressions of VEGF-A and VEGFR1 in the subperiosteal space in fracture callus. (a) Safranin-O staining of a fracture callus 10 days post fracture (10-DPF) shows a zone of intramembranous bone formation (box 1), a zone of primitive mesenchymal-appearing cells in the soft tissue callus (box 2), and an area of mature hyaline-type cartilage in the soft tissue callus (box 3). The interface between the soft tissue callus and the hard tissue callus is denoted in box 4. (b) High power photomicrographs of the 4 regions of interest stained with Safranin-O and immunofluorescence for VEGF-A (red) or VEGFR1 (yellow). (box 1) Hard tissue callus consisting of intramembranous ossification shows abundant immunoreactivity of VEGF-A primarily in the overlying periosteum and numerous VEGFR1-positive cells within the sub-periosteal space. (box 2) Safranin-O staining shows a cellular zone of primitive spindle cells without evidence of matrix deposition, in which VEGF-A or VEGFR1 is not detectable. (box 3) VEGF-A appears to be limited to occasional enlarged, hypertrophic chondrocytes within this area of hyaline cartilage. No VEGFR1 immunostaining is observed. (box 4) Abundant VEGF-A immunoreactivity is present in the stromal at the interface of the soft and hard tissue calluses, in addition to hypertrophic chondrocytes at the periphery of the avascular soft tissue callus. VEGFR1-positive cells are also present within the hard tissue callus at the transition zone. Scale bars: 20 μm.

vasculature through cortical anastomoses [53]. Thus, it is plausible that periosteal elevation results not only from traumatic hemorrhage and hematoma formation, but also from shunting the interrupted intramedullary blood flow to the regional periosteal vasculature. This theory is strongly supported by our application of novel, state of the art molecular and imaging approaches which revealed enhanced vascular anastomosis between the intramedullary vasculature and the areas of periosteal vascular engorgement during the earlier phases of fracture healing. Although these findings do not disprove the conventional hypothesis that periosteal revascularization occurs via ingrowth of vessels from the surrounding soft tissues, it does provide the first evidence that periosteal vasculature is directly connected to the intact intramedullary vasculature. Thus, we posit that shunting blood flow from the intact intramedullary vasculature to the subperiosteal space adjacent to the fracture site is an initial step displaced fracture revascularization in our model.

Formation of new bone during healing of a displaced fracture is achieved through both intramembranous and endochondral ossification. During intramembranous ossification, new bone is produced by direct extension of osteoblasts and endothelial cells [37,54,55]. Previous investigations have demonstrated that this process is tightly regulated by chemotactic and proliferative responses of endothelial cells and osteoblasts to VEGF-A through VEGF receptors including VEGFR1 [32,56–58]. In our studies, we found that the initial site of intramembranous ossification occurs at the periosteal region with the most robust expression of VEGF-A. Also, at this same location there are numerous VEGFR1 & 2-positive cells morphologically consistent with osteoblasts and endothelial cells. Based on these observations, we propose the following revisions to the current model of fracture repair: 1) the initial site of intramembranous ossification and revascularization occurs at the proximal and distal aspects of the fracture site, where periosteum inserts on adjacent uninvolved cortical bone because this is the

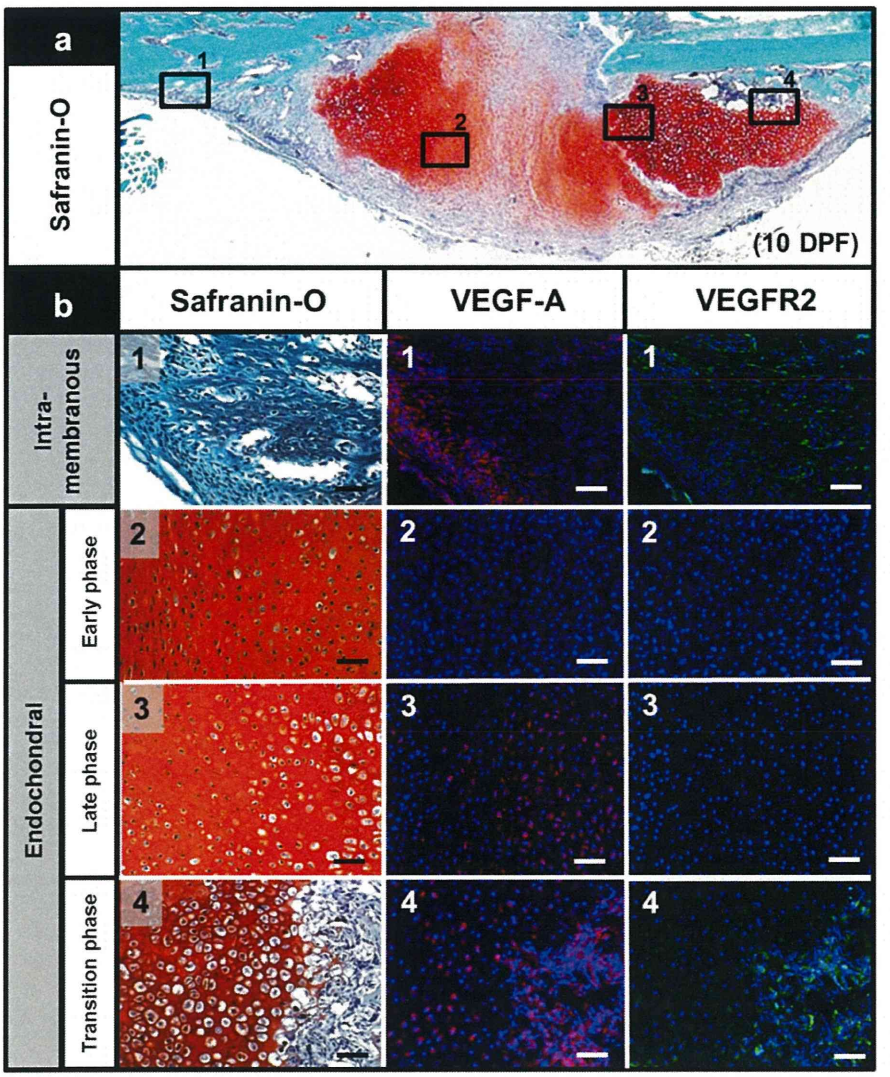

Fig. 8. Differential expressions of VEGF-A and VEGFR2 in the subperiosteal space in fracture callus. (a) Safranin-O staining of a fracture callus 10 days post fracture (10-DPF) shows a zone of intramembranous bone formation (box 1), a zone of primitive mesenchymal-appearing cells in the soft tissue callus (box 2), and an area of mature hyaline-type cartilage in the soft tissue callus (box 3). The interface between the soft tissue callus and the hard tissue callus is denoted in box 4. (b) High power photomicrographs of the 4 regions of interest stained with Safranin-O and immunofluorescence for VEGF-A (red) or VEGFR2 (green). (box 1) Hard callus consisting of intramembranous ossification shows abundant VEGF-A immunoreactivity primarily in the overlying periosteum and numerous VEGFR2-positive cells within the sub-periosteal space. (box 2) Safranin-O staining shows a cellular zone of primitive spindle cells without evidence of matrix deposition, in which VEGF-A or VEGFR2 is not detectable. (box 3) VEGF-A immunoreactivity appears to be limited to enlarged, hypertrophic chondrocytes within this area of hyaline cartilage. No VEGFR2 immunostaining is observed. (box 4) Abundant VEGF-A immunoreactivity is present in the stromal at the interface of the soft and hard tissue calluses, in addition to hypertrophic chondrocytes at the periphery of the avascular soft tissue callus. VEGFR2-positive cells are also present within the hard tissue callus at the transition zone. Scale bars: 20 μm.

site where intramedullary blood flow is shunted to the periosteum. 2) Although the initiating signal for VEGF release is not clear, the immunolocalization of VEGF-A in the periosteum at this site is likely instrumental for the recruitment and/or activation of VEGFR1 & 2-positive mesenchymal cells, endothelial cells, and osteoblasts to the subperiosteal space to support intramembranous angiogenesis and bone formation.

In contrast to intramembranous ossification, bone is formed on a pre-existing cartilaginous template during endochondral ossification [59]. In the central area of the fracture callus that is far from the disrupted regional vasculature, the initial mesenchymal cell proliferation differentiates along the chondrocyte lineage, likely due to the low oxygen tension in this avascular environment. This is supported by our angiographic and histologic data showing that the soft tissue callus is composed of avascular hyaline cartilage and primitive fibrocartilage. In addition, there was minimal detectable periosteal VEGF-A in this location and no VEGF-A positive cells were seen within the central soft callus. Thus, during the initial phases of fracture healing the central, avascular cartilaginous soft tissue callus abuts areas of richly vascular intramembranous ossification composed of VEGFR1-positive osteoblasts and endothelial cells, thereby recapitulating the primary spongiosum of the physis. Therefore, we propose that the fundamental event during fracture repair determining whether bone heals through a vascular intramembranous or an avascular endochondral pathway is its proximity to intact intramedullary vascular system and the presence of VEGFR1-positive cells.

In the active physis, expression of VEGF-A by hypertrophic chondrocytes recruits VEGFR1-positive endothelial cells and osteoblasts

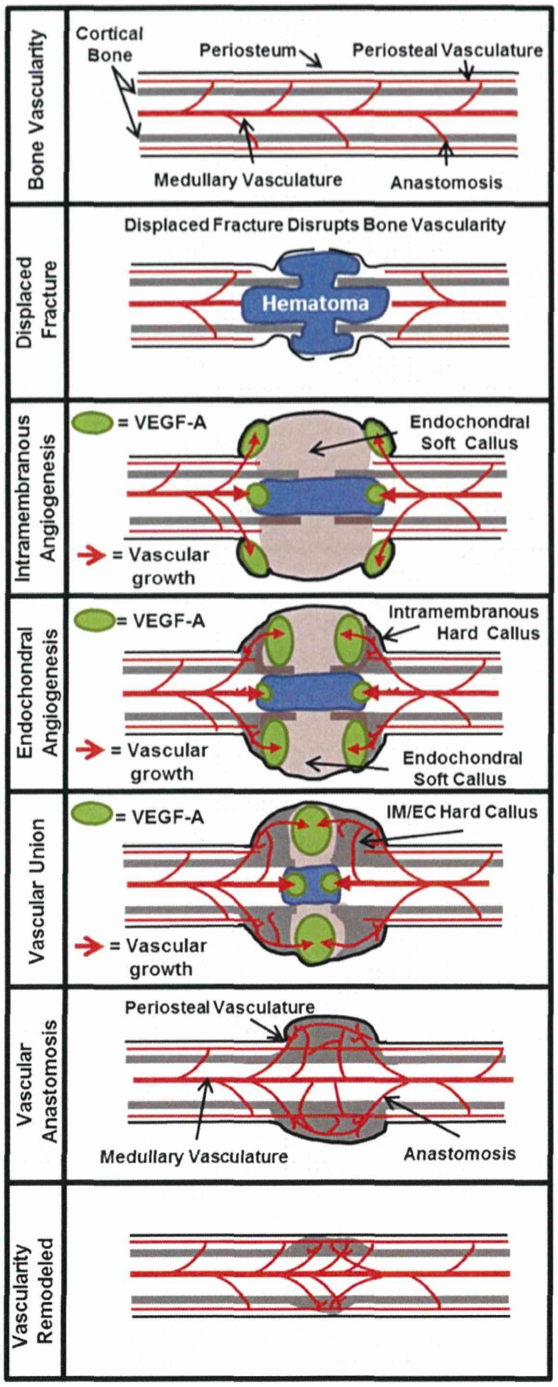

Fig. 9. Proposed model of bone revascularization during fracture healing. In a normal long bone, the intramedullary blood supply communicates with periosteal vessels. Trauma and resultant hemorrhage after acute fracture lead to regional hematoma formation, disrupting the intramedullary and periosteal vasculature. As a result of increased centrifugal flow, blood is shunted from the intramedullary vasculature to the periosteal vasculature. Subsequently, cells within the periosteum express VEGF-A and recruit endothelial cells and osteoblasts to the area. This results in the initial hard tissue callus formation through intramembranous ossification. Ordered release of VEGF-A by hypertrophic chondrocytes at the edges of the soft callus directs its replacement by nascent blood vessels and woven bone through endochondral ossification. As the extramedullary vasculature reunites with intramedullary vasculature, the newly formed blood vessels and hard callus are remodeled and resemble the original cortical bone. IM = intramembranous & EC = Endochondral.

to the zone of hypertrophy, where osteoid deposition on the cartilage matrix results in formation of the primary bone spongiosum. Indeed, the interface between soft and hard tissue calluses in a fracture site closely resembles the primary spongiosa of the physis [17,18,59–61]. In support of this, we have shown that hypertrophic VEGF-A-positive chondrocytes are present in areas of transition from avascular soft tissue callus to vascularized hard tissue callus, which are rich in VEGFR-positive cells. The essential nature of VEGF-A during fracture repair is supported by evidence that inhibiting VEGFR1 & 2 or VEGF-A impairs ossification and results in a persistent avascular soft tissue callus composed of hypertrophic chondrocytes [15,19,62]. Hence, these results indicate that 1) the VEGF-A/VEGFR system is an essential component of the transition from soft-tissue callus to hard tissue callus resulting in vascular and bone union and 2) chondrocyte hypertrophy and release of VEGF-A directs polarized bone formation through the recruitment of the vasculature and mesenchymal osteoprogenitor cells at the periphery of callus.

Our results further suggest that after union of the fracture, angiogenesis and vascular remodeling continue. Specifically, we found that fracture remodeling begins around the time at which the intramedullary vasculature is re-established. From these observations we hypothesize that fracture remodeling occurs as a result of the restoration of intramedullary vascular continuity and as normal intramedullary blood flow is re-established, periosteal shunting is reduced and the periosteal callus becomes relatively hypo-perfused. In support of this theory, Rhinelander observed that when fracture fragments are approximated such that the intramedullary vasculature directly communicates with periosteal vessels, and does not occur until re-establishment of intramedullary blood flow [31,36].

In conclusion, we have developed a model that indicates that there is an intricate interplay between intramembranous and endochondral ossification during fracture healing in young growing male mice. Periosteal intramembranous bone formation is critical in providing a richly vascularized network of osteoblastic potential that is necessary for subsequent invasion and replacement of soft tissue callus. Hypertrophic chondrocytes releasing VEGF-A in the avascular soft tissue callus seem to be required for recruiting the developing vascular network and osteoblastic mesenchymal cells to replace the soft tissue callus and form an ossified callus across the fracture site. By quantification of the phases of fracture healing over time (Fig. 3 & Table 1), we discovered that fracture revascularization is inversely proportional to the size of the soft tissue callus and directly proportional to the size of the hard tissue callus. Thus, the temporal and spatial development of fracture vascularity is controlled by the precise orchestration of intramembranous and endochondral processes.

The diseases most commonly associated with delayed fracture healing or fracture non-union all share a component of vascular dysfunction. Given this association, several investigations have proposed that addressing vascular dysfunction may significantly reduce fracture healing complications in certain patient populations [63–67]. This model of revascularization during healing of displaced/stabilized fractures identifies the specific temporal and spatial events that will provide future insight as to the causes of and potential means to prevent and treat delayed fracture healing and non-union. Additionally, while other investigations have revealed vasculature emanating from muscle surrounding a fracture [52,68], our model clearly demonstrate communication between the intramedullary vasculature and the fracture callus. Future studies are required to determine the relative significance of the contribution of intramedullary as opposed to muscle derived angiogenesis on fracture revascularization. Additionally, future studies designed to determine if the results regarding the temporal and spatial revascularization of a healing fracture are altered by the mode of fracture or in conditions known to affect bone and vascular biology such as age, sex, and chronic medical conditions such as diabetes or obesity. If so, these findings may provide insight into novel surgical and medical treatments intended to restore the normal process of bone revascularization following a fracture.

Supplementary data to this article can be found online at http://dx.doi.org/10.1016/j.bone.2014.07.002.

Acknowledgments

The authors would like to thank Craig Duvall for teaching the angiography technique used in this manuscript and David A. Haynes, Cesar Molina-Andrade, Adam Gailani, Lynda O'Rear and Marissa Mencio for their assistance with performing, imaging and attending to the mice utilized in this study. The authors would also like to thank Perry Schoenecker, Gregory Mencio, William Obremskey, Kevin O'Neill, Megan Mignemi, Richard Jacobson and Melanie Phillips for their critical review of this manuscript. This work was presented in part at the 2013 Annual Salter Lecture in Toronto, Canada, Emory Orthopaedics Grand Rounds, Atlanta, Georgia and the 2014 POSNA annual meeting.

References

[1] Praemer A, Furner S, Rice DP. American Academy of Orthopaedic Surgeons. Musculoskeletal conditions in the United States. 1st ed. Park Ridge, Ill: American Academy of Orthopaedic Surgeons; 1992.
[2] Einhorn TA. Enhancement of fracture-healing. J Bone Joint Surg Am 1995;77:940–56.
[3] Ebraheim NA, Martin A, Sochacki KR, Liu J. Nonunion of distal femoral fractures: a systematic review. Orthop Surg 2013;5:46–50.
[4] Kline AJ, Gruen GS, Pape HC, Tarkin IS, Irrgang JJ, Wukich DK. Early complications following the operative treatment of pilon fractures with and without diabetes. Foot Ankle Int 2009;30:1042–7.
[5] Cobb TK, Gabrielsen TA, Campbell II DC, Wallrichs SL, Ilstrup DM. Cigarette smoking and nonunion after ankle arthrodesis. Foot Ankle Int 1994;15:64–7.
[6] Robinson CM, Court-Brown CM, McQueen MM, Wakefield AE. Estimating the risk of nonunion following nonoperative treatment of a clavicular fracture. J Bone Joint Surg Am 2004;86-A:1359–65.
[7] Macey LR, Kana SM, Jingushi S, Terek RM, Borretos J, Bolander ME. Defects of early fracture-healing in experimental diabetes. J Bone Joint Surg Am 1989;71:722–33.
[8] Gruber R, Koch H, Doll BA, Tegtmeier F, Einhorn TA, Hollinger JO. Fracture healing in the elderly patient. Exp Gerontol 2006;41:1080–93.
[9] Ogden CL, Carroll MD, Kit BK, Flegal KM. Prevalence of obesity and trends in body mass index among US children and adolescents, 1999–2010. JAMA 2012;307:483–90.
[10] Ginter E, Simko V. Global prevalence and future of diabetes mellitus. Adv Exp Med Biol 2012;771:35–41.
[11] Rathmann W, Giani G. Global prevalence of diabetes: estimates for the year 2000 and projections for 2030. Diabetes Care 2004;27:2568–9 [author reply 2569].
[12] Etzioni DA, Liu JH, Maggard MA, Ko CY. The aging population and its impact on the surgery workforce. Ann Surg 2003;238:170–7.
[13] Christensen K, Doblhammer G, Rau R, Vaupel JW. Ageing populations: the challenges ahead. Lancet 2009;374:1196–208.
[14] Beamer B, Hettrich C, Lane J. Vascular endothelial growth factor: an essential component of angiogenesis and fracture healing. HSS J 2010;6:85–94.
[15] Gerber HP, Vu TH, Ryan AM, Kowalski J, Werb Z, Ferrara N. VEGF couples hypertrophic cartilage remodeling, ossification and angiogenesis during endochondral bone formation. Nat Med 1999;5:623–8.
[16] Harper J, Klagsbrun M. Cartilage to bone—angiogenesis leads the way. Nat Med 1999;5:617–8.
[17] Brookes M, Landon DN. The juxta-epiphysial vessels in the long bones of foetal rats. J Bone Joint Surg 1964;46:336–45.
[18] Maes C, Kobayashi T, Selig MK, Torrekens S, Roth SI, Mackem S, et al. Osteoblast precursors, but not mature osteoblasts, move into developing and fractured bones along with invading blood vessels. Dev Cell 2010;19:329–44.
[19] Hausman MR, Schaffler MB, Majeska RJ. Prevention of fracture healing in rats by an inhibitor of angiogenesis. Bone 2001;29:560–4.
[20] Burns DM. Epidemiology of smoking-induced cardiovascular disease. Prog Cardiovasc Dis 2003;46:11–29.
[21] Grundy SM, Benjamin IJ, Burke GL, Chait A, Eckel RH, Howard BV, et al. Diabetes and cardiovascular disease: a statement for healthcare professionals from the American Heart Association. Circulation 1999;100:1134–46.
[22] Meigs JB. Epidemiology of type 2 diabetes and cardiovascular disease: translation from population to prevention: the Kelly West award lecture 2009. Diabetes Care 2010;33:1865–71.
[23] Purnell JQ, Zinman B, Brunzell JD, Group DER. The effect of excess weight gain with intensive diabetes mellitus treatment on cardiovascular disease risk factors and atherosclerosis in type 1 diabetes mellitus: results from the Diabetes Control and Complications Trial/Epidemiology of Diabetes Interventions and Complications Study (DCCT/EDIC) study. Circulation 2013;127:180–7.
[24] Willigendael EM, Teijink JA, Bartelink ML, Kuiken BW, Boiten J, Moll FL, et al. Influence of smoking on incidence and prevalence of peripheral arterial disease. J Vasc Surg 2004;40:1158–65.
[25] Kolodny A. Periosteal blood supply and healing fractures. J Bone Joint Surg Am 1923;5:698–711.
[26] Teneff S. Experimental studies on vascularization of bony calluses. J Int Coll Surg 1950;13:186–91.
[27] Göthman L. Vascular reactions in experimental fractures: microangiographic and radioisotope studies. Acta Chir Scand 1961;284:1–34.
[28] Trueta J, Cavadias AX. Vascular changes caused by the Kuntscher type of nailing; an experimental study in the rabbit. J Bone Joint Surg 1955;37-B:492–505.
[29] Ladanyi J, Hidvegi E. Blood supply of experimental callus formation. Acta Morphol Acad Sci Hung 1954;4:35–44.
[30] Rhinelander FW, Baragry R. Microangiography in bone healing. I. Undisplaced closed fractures. J Bone Joint Surg Am 1962;44-A:1273–98.
[31] Rhinelander FW, Phillips RS, Steel WM, Beer JC. Microangiography in bone healing. II. Displaced closed fractures. J Bone Joint Surg Am 1968;50:643–62 [passim].
[32] Leung DW, Cachianes G, Kuang WJ, Goeddel DV, Ferrara N. Vascular endothelial growth factor is a secreted angiogenic mitogen. Science 1989;246:1306–9.
[33] Barron SE, Robb RA, Taylor WF, Kelly PJ. The effect of fixation with intramedullary rods and plates on fracture-site blood flow and bone remodeling in dogs. J Bone Joint Surg Am 1977;59:376–85.
[34] Cavadias AX, Trueta J. An experimental study of the vascular contribution to the callus of fracture. Surg Gynecol Obstet 1965;120:731–47.
[35] Rhinelander FW. The normal microcirculation of diaphyseal cortex and its response to fracture. J Bone Joint Surg Am 1968;50:784–800.
[36] Rhinelander FW. Tibial blood supply in relation to fracture healing. Clin Orthop Relat Res 1974:34–81.
[37] Stump CW. The histogenesis of bone. J Anat 1925;59:136–54.
[38] Trueta J. Appraisal of the vascular factor in the healing of fractures of the femoral neck. J Bone Joint Surg 1957;39-B:3–5.
[39] Trueta J, Amato VP. The vascular contribution to osteogenesis. III. Changes in the growth cartilage caused by experimentally induced ischaemia. J Bone Joint Surg Br 1960;42-B:571–87.
[40] Trueta J, Buhr AJ. The vascular contribution to osteogenesis. V. The vasculature supplying the epiphysial cartilage in rachitic rats. J Bone Joint Surg Br 1963;45:572–81.
[41] Trueta J, Little K. The vascular contribution to osteogenesis. II. Studies with the electron microscope. J Bone Joint Surg Br 1960;42-B:367–76.
[42] Trueta J, Morgan JD. The vascular contribution to osteogenesis. I. Studies by the injection method. J Bone Joint Surg Br 1960;42-B:97–109.
[43] Trueta J, Trias A. The vascular contribution to osteogenesis. IV. The effect of pressure upon the epiphysial cartilage of the rabbit. J Bone Joint Surg Br 1961;43-B:800–13.
[44] Doyon AR, Ferries IK, Li J. Glucocorticoid attenuates the anabolic effects of parathyroid hormone on fracture repair. Calcif Tissue Int 2010;87:68–76.
[45] O'Neill KR, Stutz CM, Mignemi NA, Burns MC, Murry MR, Nyman JS, et al. Microcomputed tomography assessment of the progression of fracture healing in mice. Bone 2012;50:1357–67.
[46] Cole HA, Yuasa M, Hawley G, Cates JM, Nyman JS, Schoenecker JG. Differential development of the distal and proximal femoral epiphysis and physis in mice. Bone 2013;52:337–46.
[47] Duvall CL, Taylor WR, Weiss D, Guldberg RE. Quantitative microcomputed tomography analysis of collateral vessel development after ischemic injury. Am J Physiol Heart Circ Physiol 2004;287:H302–10.
[48] Duvall CL, Taylor WR, Weiss D, Wojtowicz AM, Guldberg RE. Impaired angiogenesis, early callus formation, and late stage remodeling in fracture healing of osteopontin-deficient mice. J Bone Miner Res 2007;22:286–97.
[49] Dhillon RS, Xie C, Tyler W, Calvi LM, Awad HA, Zuscik MJ, et al. PTH-enhanced structural allograft healing is associated with decreased angiopoietin-2-mediated arteriogenesis, mast cell accumulation, and fibrosis. J Bone Miner Res 2013;28:586–97.
[50] Gerstenfeld LC, Cho TJ, Kon T, Aizawa T, Tsay A, Fitch J, et al. Impaired fracture healing in the absence of TNF-alpha signaling: the role of TNF-alpha in endochondral cartilage resorption. J Bone Miner Res 2003;18:1584–92.
[51] Kusumbe AP, Ramasamy SK, Adams RH. Coupling of angiogenesis and osteogenesis by a specific vessel subtype in bone. Nature 2014;507:323–8.
[52] Uhrig BA, Boerckel JD, Willett NJ, Li MT, Huebsch N, Guldberg RE. Recovery from hind limb ischemia enhances rhBMP-2-mediated segmental bone defect repair in a rat composite injury model. Bone 2013;55:410–7.
[53] Brookes M. Sequelae of experimental partial ischaemia in long bones of the rabbit. J Anat 1960;94:552–61.
[54] Brighton CT, Hunt RM. Early histologic and ultrastructural changes in microvessels of periosteal callus. J Orthop Trauma 1997;11:244–53.
[55] Percival CJ, Richtsmeier JT. Angiogenesis and intramembranous osteogenesis. Dev Dyn 2013;242:909–22.
[56] Mayr-Wohlfart U, Waltenberger J, Hausser H, Kessler S, Gunther KP, Dehio C, et al. Vascular endothelial growth factor stimulates chemotactic migration of primary human osteoblasts. Bone 2002;30:472–7.
[57] Deckers MM, Karperien M, van der Bent C, Yamashita T, Papapoulos SE, Lowik CW. Expression of vascular endothelial growth factors and their receptors during osteoblast differentiation. Endocrinology 2000;141:1667–74.
[58] Ferrara N, Henzel WJ. Pituitary follicular cells secrete a novel heparin-binding growth factor specific for vascular endothelial cells. Biochem Biophys Res Commun 1989;161:851–8.
[59] Gerstenfeld LC, Cullinane DM, Barnes GL, Graves DT, Einhorn TA. Fracture healing as a post-natal developmental process: molecular, spatial, and temporal aspects of its regulation. J Cell Biochem 2003;88:873–84.
[60] Lee FY, Choi YW, Behrens FF, DeFouw DO, Einhorn TA. Programmed removal of chondrocytes during endochondral fracture healing. J Orthop Res 1998;16:144–50.
[61] Zuscik MJ, Hilton MJ, Zhang X, Chen D, O'Keefe RJ. Regulation of chondrogenesis and chondrocyte differentiation by stress. J Clin Invest 2008;118:429–38.

[62] Jacobsen KA, Al-Aql ZS, Wan C, Fitch JL, Stapleton SN, Mason ZD, et al. Bone formation during distraction osteogenesis is dependent on both VEGFR1 and VEGFR2 signaling. J Bone Miner Res 2008;23:596–609.
[63] Groothuis A, Duda GN, Wilson CJ, Thompson MS, Hunter MR, Simon P, et al. Mechanical stimulation of the pro-angiogenic capacity of human fracture haematoma: involvement of VEGF mechano-regulation. Bone 2010;47:438–44.
[64] Paglia DN, Wey A, Breitbart EA, Faiwiszewski J, Mehta SK, Al-Zube L, et al. Effects of local insulin delivery on subperiosteal angiogenesis and mineralized tissue formation during fracture healing. J Orthop Res 2013;31:783–91.
[65] Athanasopoulos AN, Schneider D, Keiper T, Alt V, Pendurthi UR, Liegibel UM, et al. Vascular endothelial growth factor (VEGF)-induced up-regulation of CCN1 in osteoblasts mediates proangiogenic activities in endothelial cells and promotes fracture healing. J Biol Chem 2007;282:26746–53.
[66] Matsumoto T, Kawamoto A, Kuroda R, Ishikawa M, Mifune Y, Iwasaki H, et al. Therapeutic potential of vasculogenesis and osteogenesis promoted by peripheral blood CD34-positive cells for functional bone healing. Am J Pathol 2006;169:1440–57.
[67] Park AG, Paglia DN, Al-Zube L, Hreha J, Vaidya S, Breitbart E, et al. Local insulin therapy affects fracture healing in a rat model. J Orthop Res 2013;31:776–82.
[68] Morgan EF, Hussein AI, Al-Awadhi BA, Hogan DE, Matsubara H, Al-Alq Z, et al. Vascular development during distraction osteogenesis proceeds by sequential intramuscular arteriogenesis followed by intraosteal angiogenesis. Bone 2012;51:535–45.

Intrathecal AAV Serotype 9-mediated Delivery of shRNA Against TRPV1 Attenuates Thermal Hyperalgesia in a Mouse Model of Peripheral Nerve Injury

Takashi Hirai[1], Mitsuhiro Enomoto[1], Hidetoshi Kaburagi[1], Shinichi Sotome[1], Kie Yoshida-Tanaka[2], Madoka Ukegawa[1], Hiroya Kuwahara[2], Mariko Yamamoto[2], Mio Tajiri[2], Haruka Miyata[2], Yukihiko Hirai[3], Makoto Tominaga[4], Kenichi Shinomiya[1], Hidehiro Mizusawa[2], Atsushi Okawa[1] and Takanori Yokota[2]

[1]Department of Orthopaedic Surgery, Graduate School, Tokyo Medical and Dental University, Tokyo, Japan; [2]Department of Neurology and Neurological Science, Graduate School, Tokyo Medical and Dental University, Tokyo, Japan; [3]Department of Biochemistry and Molecular Biology, Nippon Medical School, Tokyo, Japan; [4]Division of Cell Signaling, Okazaki Institute for Integrative Bioscience, National Institutes of Natural Sciences, Okazaki, Japan

Gene therapy for neuropathic pain requires efficient gene delivery to both central and peripheral nervous systems. We previously showed that an adenoassociated virus serotype 9 (AAV9) vector expressing short-hairpin RNA (shRNA) could suppress target molecule expression in the dorsal root ganglia (DRG) and spinal cord upon intrathecal injection. To evaluate the therapeutic potential of this approach, we constructed an AAV9 vector encoding shRNA against vanilloid receptor 1 (TRPV1), which is an important target gene for acute pain, but its role in chronic neuropathic pain remains unclear. We intrathecally injected it into the subarachnoid space at the upper lumbar spine of mice 3 weeks after spared nerve injury (SNI). Delivered shTRPV1 effectively suppressed mRNA and protein expression of TRPV1 in the DRG and spinal cord, and it attenuated nerve injury-induced thermal allodynia 10–28 days after treatment. Our study provides important evidence for the contribution of TRPV1 to thermal hypersensitivity in neuropathic pain and thus establishes intrathecal AAV9-mediated gene delivery as an investigative and potentially therapeutic platform for the nervous system.

Received 4 March 2013; accepted 17 October 2013; advance online publication 10 December 2013. doi:10.1038/mt.2013.247

INTRODUCTION

Neuropathic pain following peripheral nerve injury is characterized by a loss of afferent sensory function as well as hyperalgesia and allodynia,[1] and available treatments are insufficient because the underlying mechanisms are poorly understood. Furthermore, a problem associated with centrally acting drugs is that they target receptors/channels that are widely expressed and are thus associated with a higher risk of adverse effects such as sedation, dizziness, somnolence, or loss of cognitive function.[2–4]

An alternative strategy for developing novel analgesics is to target receptors and ion channels that respond to noxious stimuli at peripheral terminals of primary sensory neurons, whose cell bodies are located in the dorsal root ganglia (DRG), to produce hyperexcitability and spontaneous firing in neuropathic pain. These receptors and ion channels are selectively or primarily expressed in primary sensory neurons in the periphery,[5] which reduces the potential for side effects when they are specifically targeted by drugs. As a treatment target, vanilloid receptor 1(TRPV1) has been well characterized as a sensory transducer in nociceptors and shown to contribute to the development of mechanical and/or heat hypersensitivity under various acute pain conditions.[6] However, how TRPV1 contributes to chronic hypersensitivity induced by nerve injury (*i.e.*, neuropathic pain) remains unclear, although various TRPV1 antagonists are under clinical development based on the hypothesis that TRPV1 is involved in persistent pain, especially in thermal hyperalgesia in inflammatory pain states.[7] Further development of clinical therapeutics will be therefore facilitated by the elucidation of the role of TRPV1 in neuropathic pain; however, such an investigation first requires the development of a technology to reliably and specifically modulate TRPV1 activity *in vivo* in the peripheral nervous system/central nervous system (CNS).

RNA interference has emerged as a potent tool to investigate the specific effects of proteins by suppressing their expression, and recent work in the field of drug delivery has addressed the delivery of synthetic short interfering RNA (siRNA) across the blood–brain barrier. Nonviral systems including hydrodynamic injection, cationic liposomes,[8] nanoparticles,[9] and lipid conjugation[10] provide effective and relatively safe delivery of nucleic acids to the CNS. In comparison with viral vectors, however, they still show low transduction efficiency, insufficient inhibition of gene expression and a short duration of therapeutic effects; therefore, viral vectors may be preferable for treating chronic pain states. In particular, viral delivery of short-hairpin RNA (shRNA) expression cassettes that support efficient and long-lasting RNA interference

Correspondence: Mitsuhiro Enomoto, Department of Orthopedic Surgery, Graduate School, Tokyo Medical and Dental University, 1-5-45, Yushima, Bunkyo-ku, Tokyo 113-8519, Japan. E-mail: enomorth@tmd.ac.jp or Takanori Yokota, Department of Neurology and Neurological Science, Graduate School, Tokyo Medical and Dental University, 1-5-45, Yushima, Bunkyo-ku, Tokyo 113-8519, Japan. E-mail: yokonuro@tmd.ac.jp

is expected open new frontiers for molecular therapy of the CNS.[11] We previously reported that intrathecal administration of shRNA expressed by an adenoassociated virus serotype 9 (AAV9) vector produced long-term suppression of target gene expression in both the DRG and spinal cord without neurologic side effects or toxicity,[12] which suggests that this approach can be used to modulate the expression of genes involved in neuropathic pain states. Thus, in the present study, we used intrathecal administration of AAV9 encoding shRNA targeting TRPV1 in a mouse model of spared nerve injury (SNI) to test the hypothesis that TRPV1 plays a critical role in neuropathic pain.

RESULTS

Design, selection, and validation of siRNA sequences against TRPV1 for construction of AAV9 shTRPV1

Seven candidate siRNA sequences for TRPV1 were designed from the TRPV1 coding sequence (NM_001001445.1, **Figure 1a**). The silencing efficacy of these sequences was determined using

a

Names	siRNA sequences targeting TRPV1
1	5′ -GGCCAGACAGCAUUACACATT- 3′
	3′ -TTCCGGUCUGUCGUAAUGUGU- 5′
2	5′ -GCCACGACAUGCUUCUUGUTT- 3′
	3′ -TTCGGUGCUGUACGAAGAACT- 5′
3	5′ -GGCGCAUCUUCUACUUCAATT- 3′
	3′ -TTCCGCGUAGAAGAUGAAGUU- 5′
4	5′ -GCGCAUCUUCUACUUCAACTT- 3′
	3′ -TTCGCGUAGAAGAUGAAGUUG- 5′
5	5′ -GAGACCUGUGUCGGUUUAUTT- 3′
	3′ -TTCUCUGGACACAGCCAAAUA- 5′
6	5′ -GUCGGUUUAUGUUCGUCUATT- 3′
	3′ -TTCAGCCAAAUACAAGCAGAU- 5′
7	5′ -GGCCAGGUAACUCUUACAATT- 3′
	3′ -TTCCGGUCCAUUGAGAAUGUU- 5′
SC	5′ -GUACCGCACGUCAUUCGUATT - 3′
	3′ -TTCAUGGCGUGCAGUAAGCAU - 5′

b

Names	siRNA sequences targeting TRPV1
A	5′-GTCGGTTTATGTTCGTCTAC-3′
B	5′-GTTGGTTTGTGTTCGTCTGC-3′
SC	5′-TAGCGTAAGTGATTAACTAC-3′

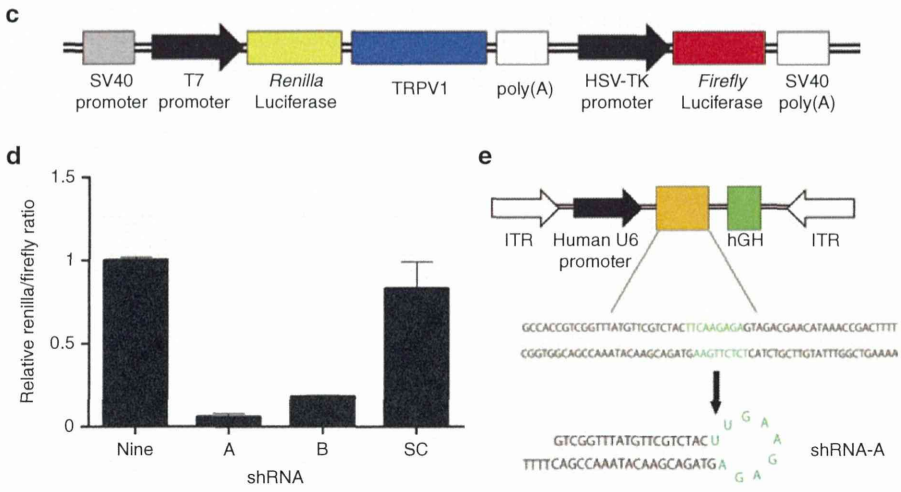

Figure 1 Selection of siRNA-E sequence for insertion into the AAV9 vector. (**a**) Small interfering RNA sequences targeting TRPV1. (**b**) Short-hairpin RNA (shRNA) sequences targeting TRPV1. (**c**) Schematic representation of the plasmid vector used *in vitro*. This plasmid encodes *firefly* luciferase and a fusion *renilla* luciferase and TRPV1. (**d**) Relative TRPV1 expression level *in vitro* as determined by *renilla*/*firefly* ratio. Data are presented as means ± SEM. (**e**) The AAV9-shTRPV1 vector, including the shRNA sequence driven by the human polymerase III human U6 promoter and hGH inserted downstream of the shRNA sequence for the AAV9 genome detection assay, is shown. AAV, adenoassociated virus; hGH, human growth hormone; HSV-TK, herpes simplex virus-thymidine kinase; ITR, inverted terminal repeat; SC, scramble; SV, Simian virus; TRPV1, transient receptor potential vanilloid 1.

a luciferase assay *in vitro* as described below. Subsequently, we selected the one siRNA sequence out of seven candidates that had the highest efficiency, and then two sequences were designed for inclusion in the shRNA expression vector (**Figure 1b**).

The selected seven siRNA and two shRNA molecules were tested individually for knockdown efficiency in cultured human embryonic kidney (HEK)293T cells that were transfected with a plasmid vector encoding of *renilla* luciferase with TRPV1 in its 3′ untranslated region as well as *firefly* luciferase as a transfection control (**Figure 1c**). Among the seven siRNA sequences, siRNA-6 reduced *renilla* luciferase activity (used as a proxy for TRPV1 expression) by ~90% relative to *firefly* luciferase activity, whereas the other sequences reduced *renilla* luciferase activity by ~70–80%. *Renilla* luciferase activity was not significantly altered by transfection with siRNA containing a scrambled sequence. Two putative shRNA sequences were therefore designed based on the siRNA-6 sequence. Between the two shRNA sequences, shRNA-A was more effective, as it reduced *renilla* luciferase activity by ~95% relative to *firefly* luciferase activity (**Figure 1d**) and was thus selected for further experiments and inserted downstream of the human polymerase III U6 promoter in the AAV9 vector (**Figure 1e**).

TRPV1 mRNA expression is significantly increased in the lumbar DRG and spinal cord following SNI

We first confirmed the development of hypersensitivity in the hindpaw of SNI mice (**Figure 2a**).[13] Behavioral testing was

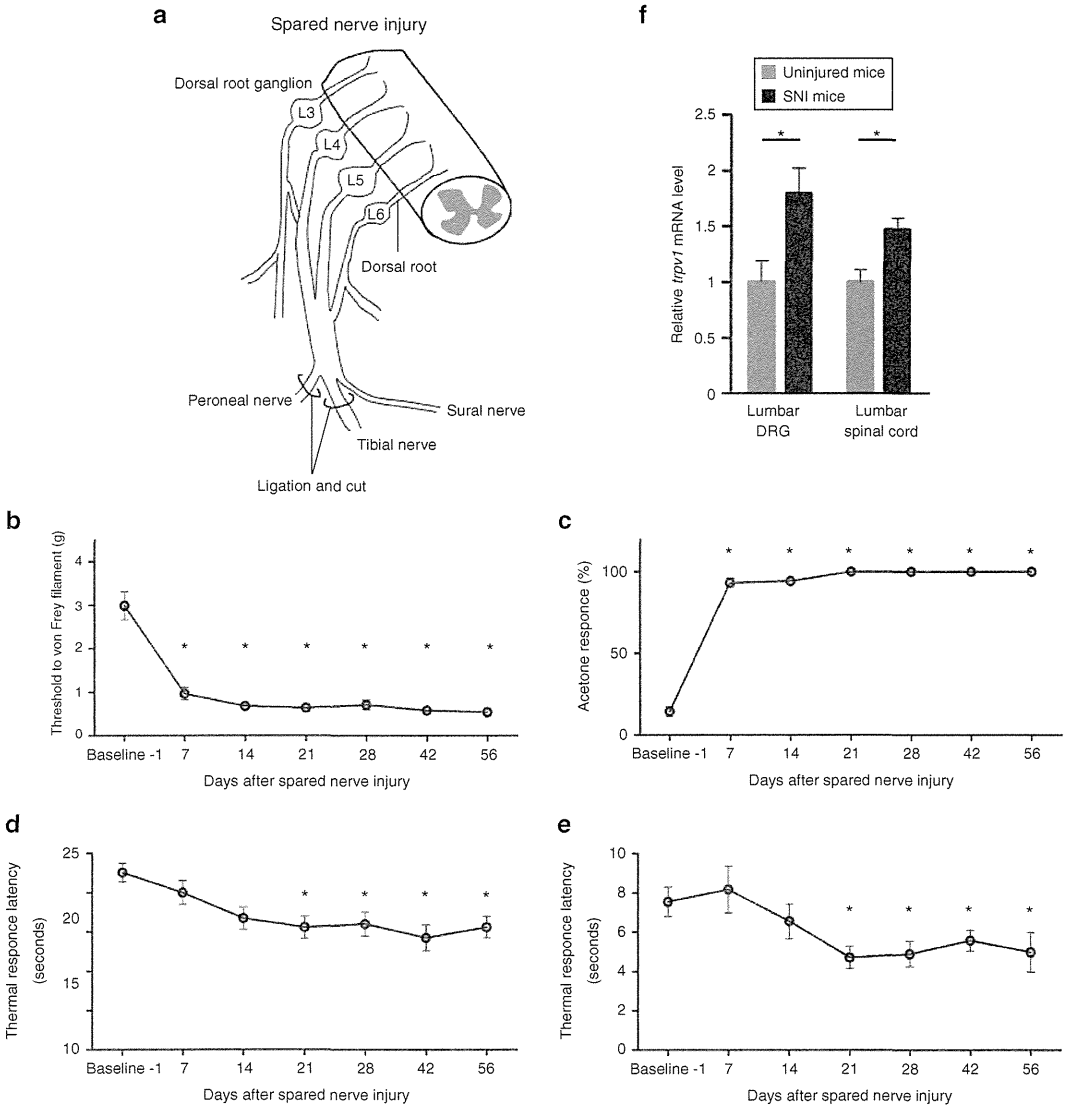

Figure 2 Time course of mechanical, cold, and heat sensitivity following spared nerve injury. (**a**) Schematic representation of the spared nerve injury model showing ligation of the tibial and common peroneal nerves distal to the trifurcation. Spared nerve injury resulted in immediate mechanical (**b**) and cold (**c**) hypersensitivity. Latencies to heat stimulation at 50 and 55 °C decreased gradually and were significantly lower at 3 weeks after nerve injury than at (**d** and **e**) baseline. (**f**) Quantitative reverse transcription polymerase chain reaction analysis showed that *trpv1* expression at 3 weeks after nerve injury was 179±23% ($P < 0.05$) in the DRG and 147±10% ($P < 0.05$) in the spinal cord relative to tissues from uninjured mice. Data are presented as means ± SEM (n = 6–18 mice per group; $P < 0.05$). *trpv1*, transient receptor potential vanilloid 1.

performed on the lateral side of the plantar hindpaw, which is completely innervated by the spared sural nerve.

Within 3 weeks after nerve injury, the mice exhibited tactile hyperalgesia in response to probing by Von Frey filaments, cold hyperalgesia in response to acetone, and thermal hyperalgesia in response to contact with a hotplate (50 or 55 °C; **Figure 2b–e**). The behavioral hypersensitivity lasted until 8 weeks after SNI. However, there was no decrease in the latency of withdrawal to radiant heat stimulation, as reported previously (data not shown).[13]

The expression of *trpv1* was investigated in the ipsilateral L5 and L6 DRGs and the ipsilateral L1-L2 spinal cord (which receives input from the L5 and L6 spinal nerves), before and after SNI by quantitative reverse transcription polymerase chain reaction (RT-PCR) analysis. Three weeks after SNI, the relative *trpv1* expression as a percentage of *gapdh* expression was 179±23% in the DRG and 147±10% in the spinal cord relative to tissues from uninjured mice (**Figure 2f**), which indicates that *trpv1* was upregulated by SNI.

Thermal analgesic effect of AAV9 encoding shRNA against TRPV1 in mice with SNI

AAV9 vectors targeting TRPV1 (AAV9-shTRPV1) or superoxide dismutase 1 (AAV9-shSOD1), or phosphate-buffered saline (PBS) in the vehicle-only group, were injected intrathecally at the second lumbar vertebra of mice 3 weeks after SNI (**Figure 3a**). Because we previously demonstrated that intrathecal injection of AAV9-shSOD1 did not produce behavioral changes in mice,[14]

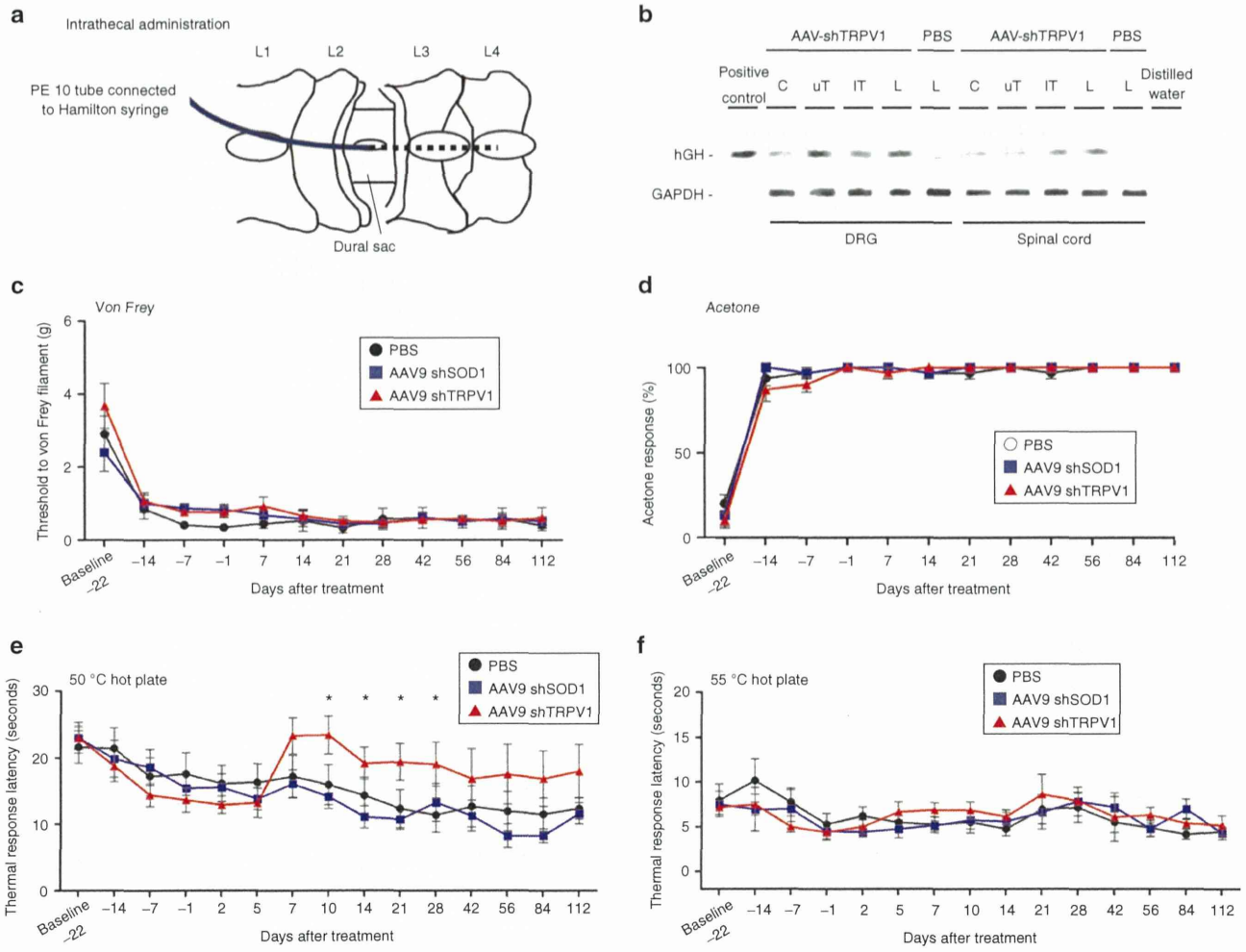

Figure 3 TRPV1 knockdown via intrathecal delivery of AAV9-shTRPV1 partially attenuates spared nerve injury (SNI)-induced thermal hyperalgesia. (**a**) Three weeks after injury, a PE-10 catheter was inserted into the subarachnoid space caudally between the L2 and L3 vertebrae following fenestration, and AAV9 or phosphate-buffered saline (PBS) was injected using a Hamilton syringe connected to the catheter. (**b**) One week after intrathecal injection of AAV9 at the lumbar spine level, high levels of AAV9 genomic DNA were detected in the upper thoracic and lumbar DRGs and lower thoracic and lumbar spinal cord, whereas low expression was observed at other levels. (**c**) Withdrawal threshold for von Frey filaments, (**d**) response to acetone application and latency of response to (**e**) 50 °C and (**f**) 55°C heat stimulation. No significant differences were observed among the three groups for withdrawal thresholds in response to (**c**) mechanical, (**d**) cold, and (**f**) 55 °C heat stimulation. (**e**) However, a partial but significant attenuation of thermal hyperalgesia in response to 50 °C heat stimulation was observed for animals injected with AAV9-shTRPV1 from day 10 to day 28 relative to the other two groups. Data are represented as means ± SEM ($n = 9$ mice per group; $P < 0.05$). AAV, adenoassociated virus; Cs, cervical; ITs, lower thoracic; Ls, lumbar; PBS, phosphate-buffered saline; SOD1, superoxide dismutase 1; TRPV1, transient receptor potential vanilloid 1; uTs, upper thoracic.

AAV9-shSOD1 was used as a negative control vector in this study. To analyze the distribution of AAV9 in the DRG or spinal cord after intrathecal injection, we performed genomic PCR to detect human growth hormone cassette (**Figure 1e**), whose sequence had been inserted into the AAV9 genome. Based on the detection of the human growth hormone sequence, higher levels of AAV9 genomic DNA were present in the upper thoracic and lumbar DRGs and lower thoracic and lumbar spinal cord than in other regions (**Figure 3b**).

To determine whether the knockdown of TRPV1 alleviated neuropathy-induced hindpaw hypersensitivity, the Von Frey, acetone, and hot plate assays were performed at various time points after intrathecal injection of the AAV9 vector. The paw withdrawal thresholds in response to mechanical (**Figure 3c**), cold (**Figure 3d**) and 55 °C thermal stimuli (**Figure 3f**) showed no obvious change in each group after treatment, and there were no significant differences among the three groups except for in the response to thermal stimulation at 50 °C. In the 50 °C thermal hot plate test, the latency to hindpaw withdrawal in the AAV9-shTRPV1 group was significantly increased from day 10 to day 28 after treatment, relative to the other two groups (**Figure 3e**).

TRPV1 expression in the spinal cord and DRG, and treatment efficacy after lumbar intrathecal administration of AAV9 shRNA against TRPV1

Quantitative RT-PCR analysis showed that the expression of *trpv1* in the AAV9-shTRPV1-treated group was ~55% lower in the DRGs and 95% lower in the lumbar spinal cord relative to PBS-treated animals at 4 weeks after injection (**Figure 4a**). The knockdown effect appeared to be specific for the target gene *trpv1*, given that the mRNA levels of *gapdh* and transthyretin (*ttr*) did not change (**Figure 4b**). Furthermore, a western blot analysis confirmed significantly decreased TRPV1 protein levels in the lumbar DRGs and spinal cord of AAV9-shTRPV1-treated mice at the same time point (**Figure 4c**).

To evaluate the efficacy of the AAV9-shTRPV1 treatment, we analyzed the relationship between the analgesic effect and the expression of *trpv1* in the AAV9-shTRPV1 group. There was a significant correlation between the analgesic effect and *trpv1* expression in the lumbar DRGs (**Figure 4d**; $Y = -36.64X+32.70$; R^2: 0.94, $P < 0.01$) and spinal cord (**Figure 4e**; $Y = -17.2X+11.91$; R^2: 0.79, $P < 0.01$).

Duration of silencing by shRNA against TRPV1 in the lumbar DRGs and spinal cord

We evaluated the duration of TRPV1 suppression by the AAV9-shTRPV1 vector by measuring the mRNA and protein levels of TRPV1 in the lumbar DRG and spinal cord. Quantitative PCR showed that *trpv1* was reduced by 55 and 95% at 28 days, 36 and 5% at 56 days, and 37 and 0% at 84 days, respectively (**Figure 5a**). TRPV1 protein expression in both the lumbar DRGs and spinal cord was obviously inhibited at 28 days but returned to the baseline by 56 days after AAV9-shRNA injection (**Figure 5b**). These results indicate that the AAV9-shTRPV1 vector provides significant suppression of *trpv1* mRNA and protein expression in the DRG and spinal cord for at least 1 month, but *trpv1* mRNA and protein expression in the spinal cord return to baseline levels within by 2 months.

Body weight and laboratory data

To assess the general health of our mice after the therapeutic injection, we observed them for 16 weeks after treatment. The body weight was similar among the three groups (**Figure 6a**). In addition, biochemical analysis of serum components including albumin, aminotransaminases, alkaline phosphatase, blood urea nitrogen, and creatinine did not show any marked abnormalities at both 24 hours and 16 weeks after AAV9 injection (**Table 1**).

Immune response to AAV9-shTRPV1

To evaluate potential inflammatory reactions in the lumbar DRGs and spinal cord after intrathecal injection of the AAV9-shTRPV1 vector, we measured the expression of interferon using quantitative RT-PCR 24 hours after injection. Injection of AAV9-shTRPV1 did not result in increased expression of *interferon β* (*ifnβ*) mRNA relative to the PBS-treated group in either DRG or spinal cord (**Figure 6b**). To further evaluate potential immune responses to repeat injection of AAV9-shTRPV1, *ifnβ* mRNA was also measured 24 hours after the second intrathecal injection, which was performed 28 days after the first injection. The repeated injection did not lead to a significant increase in *ifnβ* mRNA levels in either the lumbar DRGs or spinal cord (**Figure 6c**). In addition, we evaluated CD8 expression in the DRG and spinal cord to determine whether a cellular immune response to AAV9-shTRPV1 occurs after single or repeated injection. Immunohistochemistry indicated a lack of $CD8^+$ cells in the lumbar DRG and spinal cord after either single administration (**Figure 6d–i**) or repeat administration of either AAV9-shTRPV1 or AAV9-shSOD1 (**Figure 6j–o**).

DISCUSSION

It is well known that several members of the transient receptor potential (TRP) family function as sensory transducers in nociceptive neurons and play important roles in the development of pathological hypersensitivity under various pain conditions. In particular, TRPV1, which is activated by various exogenous stimuli such as capsaicin, heat, protons, and spider toxins, is expressed in most small-diameter sensory fibers, *i.e.*, unmyelinated C fibers and finely myelinated Aδ fibers, whose physiological role is to detect noxious stimuli.[14] Several inflammatory conditions increase the expression of TRPV1 and even increase the density of TRPV1-positive axons.[15] Conversely, in neuropathic pain states, the role of TRPV1 is controversial, even though analgesic effects of TRPV1 antagonists have been reported. Although the total expression level of TRPV1 in the DRG tends to decrease in most neuropathic pain models, *e.g.*, chronic constriction injury,[16] partial nerve ligation,[17] and spinal nerve ligation,[18] TRPV1 is upregulated in surviving DRG somata after partial nerve ligation[17] and L4 DRG neurons after L5 spinal nerve ligation surgery.[19] In human neuropathic pain states, TRPV1 expression increases in spared peripheral nerves after injury.[20]

In the present study, we found that *trpv1* mRNA expression increased by 79 and 47% in the lumbar DRGs and spinal cord, respectively, at 3 weeks after SNI relative to the uninjured condition (**Figure 2f**). Our observations are consistent with previous findings that activation of TRPV1 in spared DRG neurons after nerve injury results in hyperalgesia.[21] In addition to the peripheral axons of primary neurons, TRPV1 is also found in the central

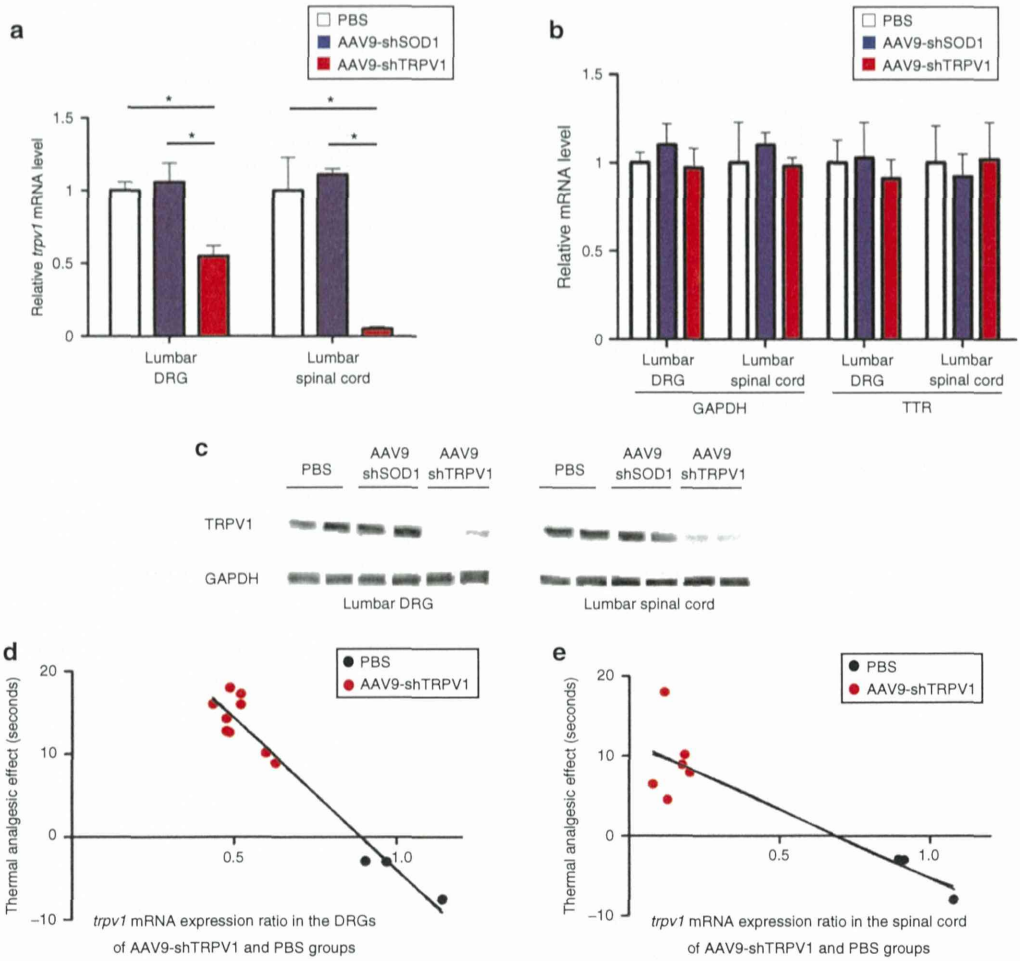

Figure 4 Intrathecal administration of AAV9-shTRPV1 specifically suppresses *trpv1* mRNA and TRPV1 protein expression *in vivo*. (**a**) Quantitative reverse transcription polymerase chain reaction (RT-PCR) analysis of *trpv1* mRNA expression in lumbar dorsal root ganglia (DRG) and spinal cord in mice 4 weeks after intrathecal injection of phosphate-buffered saline (PBS) (control), AAV9-shSOD1 or AAV9-shTRPV1. *trpv1* mRNA expression was significantly (*$P < 0.05$) inhibited in the lumbar DRG and spinal cord of the AAV9-shTRPV1-treated group relative to the two other groups. (**b**) Quantitative RT-PCR analysis of the expression of non-targeted *ttr* and *gapdh* mRNA in the lumbar DRG and spinal cord at 4 weeks after the treatment. No significant differences were found in the expression of *ttr* and *gapdh* mRNA among the three groups. Data are presented as means ± SEM ($n = 4$ or 5 mice per group; *$P < 0.05$). (**c**) TRPV1 protein levels in the lumbar DRG and spinal cord of two mice from each group, as assessed by Western blot analysis 4 weeks after treatment. A robust reduction of TRPV1 protein levels in both the DRG and spinal cord was observed in the AAV9-shTRPV1-treated group. (**d**) and (**e**) Relationship between thermal analgesia and *trpv1* mRNA expression in the lumbar DRG and spinal cord. Analgesia in response to 50 °C thermal stimulation was significantly correlated with *trpv1* mRNA expression in the lumbar DRG ($Y = -36.64X+32.70$; R^2: 0.94, $P < 0.01$) and spinal cord (**e**, $Y = -17.2X+11.91$; R^2: 0.79, $P < 0.01$).

terminals of nociceptive neurons that synapse on neurons in the dorsal horn of the spinal cord.[22] Activation of presynaptic TRPV1 in the dorsal horn by peripheral nerve injury results in increased synaptic release of glutamate and neuropeptides.[23,24] Furthermore, postsynaptic TRPV1 in GABAergic spinal interneurons mediates neuropathic mechanical allodynia and disinhibition of nociceptive circuitry including spinothalamic projections to the ventral posterior lateral nucleus of the thalamus.[25] Because neuropathic TRPV1 upregulation occurs in both the DRG and spinal cord, downregulation of TRPV1 in the peripheral nervous system and CNS may provide effective treatment of persistent pain. In the present study, intrathecal AAV9-mediated delivery of shRNA provided significant silencing of TRPV1 not only in the peripheral nervous system but also in the CNS, thereby alleviating nerve injury-induced hyperalgesia in a mouse model of peripheral neuropathic pain.

The excitation, desensitization, and neurotoxicity produced by capsaicin, which is a ligand for the TRPV1 receptor, are known to have analgesic effects. Additionally, systemic administration of resiniferatoxin, which is an ultrapotent TRPV1 agonist, to adult rats desensitizes TRPV1-positive fibers to produce long-lasting relief of thermal hyperalgesia in a neuropathic pain model.[26] However, it has also been shown that genetic knockout of TRPV1 does not affect hypersensitivity following nerve injury,[27] even though TRPV1 antagonists have been shown to reduce hypersensitivity in neuropathic pain models.[28] Accordingly, given the conflicting findings in the literature and lack of consensus in the field, we pursued the AAV-mediated knockdown of TRPV1 via RNA interference to confirm the contribution of TRPV1 to neuropathic pain behavior, particularly pain produced by noxious heat and also to develop a platform for potential therapeutic intervention.

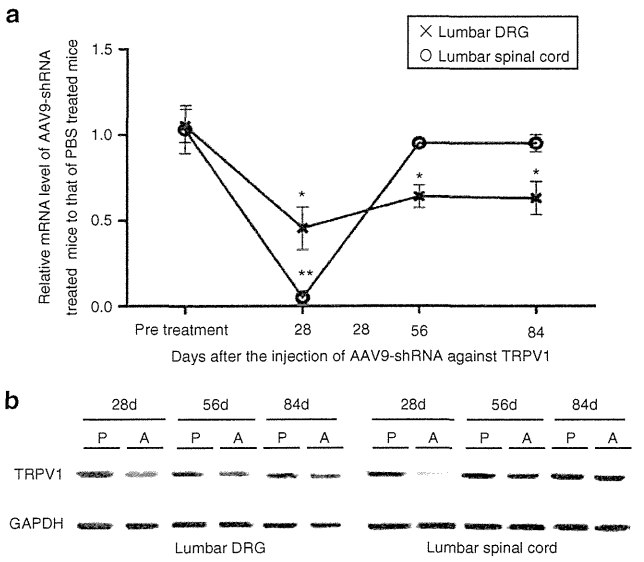

Figure 5 Duration of shRNA-mediated silencing of TRPV1 in the lumbar dorsal root ganglia (DRGs) and spinal cord. (**a**) Significant suppression of *trpv1* mRNA lasted for 3 months with a reduction of ~35% in the lumbar DRG. In lumbar spinal cord, a 95% reduction was observed at 1 month after injection, but *trpv1* mRNA expression returned to the level observed in phosphate-buffered saline (PBS)-treated mice by 2 months after injection (* denotes significant difference in the DRG *trpv1* mRNA expression, $P < 0.05$; ** denotes significant difference in spinal cord *trpv1* mRNA expression, $P < 0.05$). (**b**) TRPV1 protein expression analysis based on western blot. TRPV1 protein expression in both the lumbar DRGs and spinal cord was obviously decreased at 28 days after AAV9-shTRPV1 injection but returned to the baseline by 56 days after injection. AAV, adenoassociated virus; P, PBS-treated mice; A, AAV9-shTRPV1-treated mice; TRPV1, transient receptor potential vanilloid 1.

Several previous studies reported that RNAi-mediated suppression of TRPV1 in sensory afferent components including the DRG and spinal cord alleviated both mechanical and thermal hyperalgesia in animal models of neuropathic pain;[25,29] however, the present study showed that specific knockdown of TRPV1 reversed thermal hyperalgesia but did not affect mechanical or cold hyperalgesia. The discrepancy between our findings and those of previous studies may be the result of differences in the nerve injury models, as different animal models of neuropathic pain have been found to yield different degrees of hypersensitivity.[30] Our findings suggest that tactile and cold hypersensitivity are mediated by molecules other than TRPV1, which is logical given the specific physiological role of TRPV1 as a heat sensor.[27]

In contrast to the improvement observed at 50 °C, we found that AAV9-shTRPV1 injected intrathecally did not ameliorate thermal hyperalgesia at 55 °C, possibly because the response at 55 °C may rely on a different population of ion channels. Consistent with these findings, TRPV1 has been shown to be essential for the development of sensitization to thermal stimuli during inflammation but not for the normal sensation of noxious heat.[31] The detection of noxious heat has been proposed to be mediated by several ion channels in addition to TRPV1, including TRPV2, TRPV3, TRPV4, TRP melastatin 2 (TRPM2), and TRPM3.[32–36] Heat-evoked TRPV1 currents *in vitro* are activated at a threshold of >40 °C, increase linearly up to 50 °C, and decrease at temperatures higher than 50 °C. Although only a few receptors other than TRPV1, such as TRPM3 and ANO1,[36,37] contribute to heat sensation in the temperature range of 43–50 °C, even a partial reduction of TRPV1 expression would be expected to decrease the nocifensive response to heat in this temperature range. However, it remains unclear what molecules are involved in heat sensation, thermal nociception and hyperalgesia at temperatures higher than 50 °C, although it is possible that TRPV1 plays a minimal role because TRPV1-independent inflammatory hyperalgesia at 56 °C was previously observed in rats treated with resiniferatoxin and shown to be mediated by TRPV2.[38] Although that study and others[27]showed that TRPV2 was activated by noxious heat at temperatures higher than 50 °C *in vivo*, TRPV2 was recently shown not to be essential for heat hypersensitivity in a study using TRPV2 knockout mice.[39] Other possible candidate channels include TRPV3 and TRPM3, which were individually shown in knockout mice to contribute to thermal hypersensitivity at >52 °C but not 50 °C.[36,40] Thus, our findings shed light on the currently controversial role of TRPV1 in neuropathic pain by demonstrating that nerve injury-induced overexpression of TRPV1 indeed plays an important role in persistent pain but only in thermal hyperalgesia in response to moderate heat. Our findings also indicate that a single administration of AAV9-shTRPV1 leads to robust and relatively long-lasting suppression of TRPV1 in SNI mice (in which TRPV1 expression is significantly increased), thus resulting in a significant antinociceptive effect.

Gene therapy using AAV vectors has been increasingly applied to treat refractory neurologic disorders, and human clinical trials have suggested that recombinant AAV vectors are safe and well tolerated.[41–43] We previously reported that intrathecal delivery of AAV9 in mice was associated with little or no immunogenicity, inflammation or toxicity in terms of neurologic dysfunction or micro-RNA maturation.[12] In the current study, the interferon-β mRNA expression profile and lack of $CD8^+$ inflammatory cells suggests a relative lack of inflammation in the DRGs and spinal cord after either a single or repeated intrathecal injection of the AAV9-shTRPV1 vector. This finding is consistent with previous reports in which AAV9 was reported to lower immunoreactivity than other AAV serotypes.[44] However, the lack of an immune response in mice does not necessarily exclude the potential for immunogenicity in humans. Therefore, future investigations of the immune response to AAV9 are necessary in primates to validate the safety of the AAV9 vector for human clinical trials, and it may be necessary to engineer capsid sequences to prevent potential immune responses.[45]

In the present study, we did not observe adverse side effects on liver function or deterioration of the general condition after viral vector injection. However, in situations where side effects of shRNA expression or gene suppression are suspected or expected, strategies for tuning shRNA expression, such as the use of a tetracycline-inducible promoter for regulated expression, may be applied to increase safety.[46] Such approaches allow expression of the shRNA to be switched on temporarily through the systemic addition of doxycycline and switched off when necessary (*e.g.*, when the silencing effect is excessive or shRNA toxicity is observed) by withdrawal of doxycycline. Thus, the silencing effect on the target gene after intrathecal injection of shRNA-AAV9 may be adjusted on demand through the use of an inducible promoter. In the present study, we did not assess the therapeutic window of

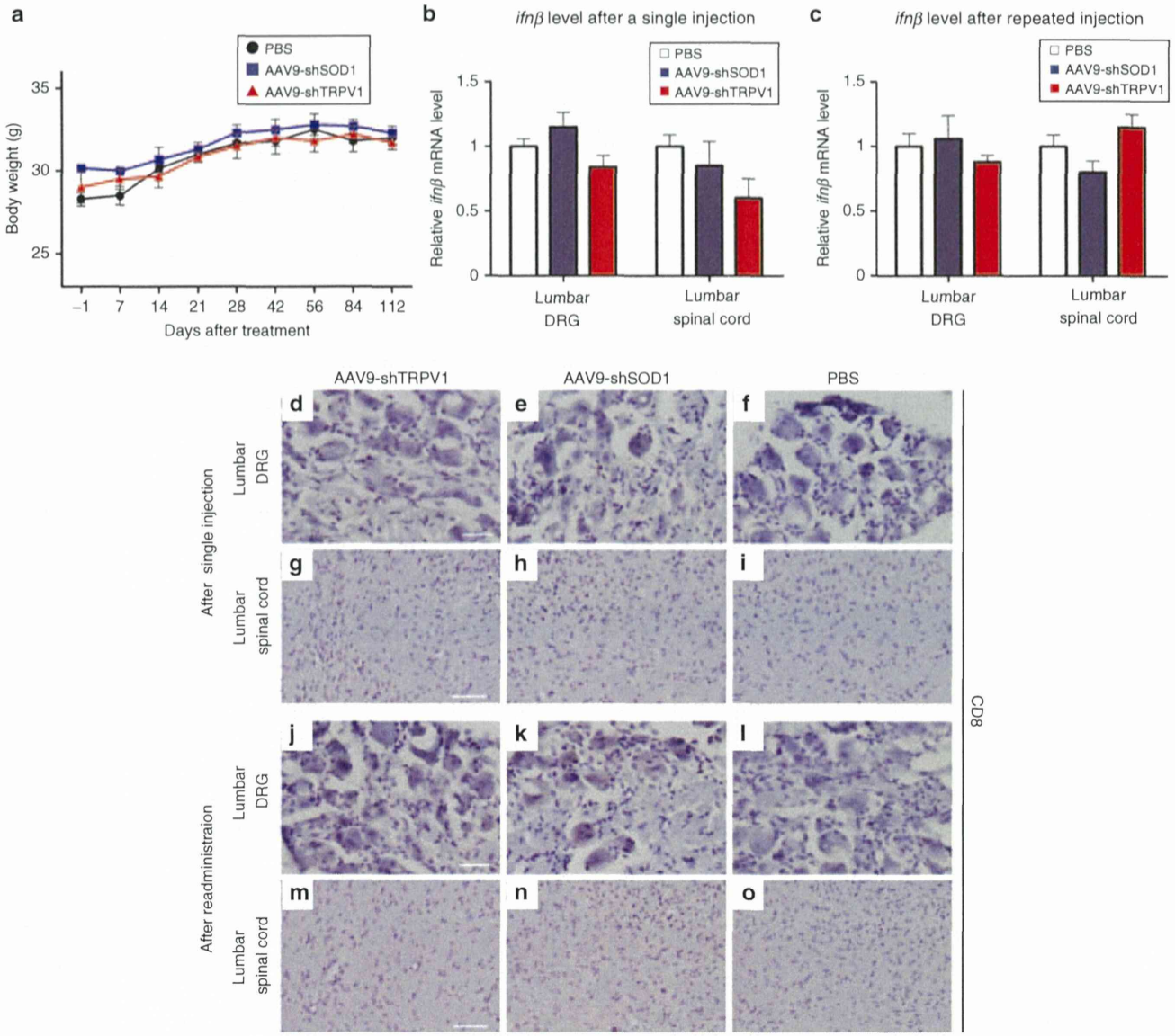

Figure 6 Assessment of body weight, inflammation, and immune response in phosphate-buffered saline (PBS), AAV9-shSOD1, and AAV9-shTRPV1-treated mice. (**a**) Throughout the 16-week experimental period, the body weight remained similar in the three treatment groups. Data are presented as means ± SEM (n = 9 mice per group). (**b**) Quantitative reverse transcription polymerase chain reaction analysis of *ifnβ* mRNA expression in lumbar dorsal root ganglia (DRG) and spinal cord in mice at 24 hours after intrathecal injection of PBS, AAV9-shSOD1, or AAV9-shTRPV1. There were no significant increases in *ifnβ* mRNA expression in the lumbar DRS and spinal cord of AAV9-shTRPV1-treated mice relative to PBS-treated mice. (**c**) Similarly, *ifnβ* mRNA expression after repeated injection of AAV9-shTRPV1 did not increase relative to that in PBS- or AAV9-shSOD1- injected mice. (**d–o**) Immunohistochemistry of CD8 expression in the lumbar DRG and spinal cord after either single (**d–i**) or repeated injection (**j–o**) of PBS, AAV9-shSOD1, or AAV9-shTRPV1. Few or no $CD8^+$ cells were observed in the lumbar DRG or spinal cord after either single or repeated administration of AAV9-shTRPV1. Bar = 20 μm for **d–f** and **j–l**; bar = 100 μm for **g–i** and **m–o**.

the shRNA encoded by the viral vector, although we confirmed that the gene-silencing effect in the DRG and spinal cord persisted for as long as 4 weeks in our mice; we therefore expect that this technique could be used for stable, long-term analgesia. Given our demonstration of AAV9's high affinity for central and peripheral nervous systems, effective transduction to drive long-term stable expression of transgenes in the DRG and spinal cord and apparent lack of systemic immunogenicity, we propose that intrathecal administration of AAV9 can be developed for clinical application to various neurologic disorders such as neurodegenerative diseases and cancer pain as well as neuropathic pain after nerve injury.

Although further studies are needed for optimization, our findings therefore establish that TRPV1 overexpression is responsible for a subset of thermal hyperalgesia in neuropathic pain that can be reversed by minimally invasive intrathecal AAV9-mediated RNA interference. Moreover, we believe that this technique can be developed as a platform technology to treat various other neuropathic pain conditions by modifying the shRNA sequence to target other molecules, including neurotrophic factors (*e.g.*, nerve

Table 1. Laboratory data in each group at 24 hours and 16 weeks after injection

Group	Alb (g/dl)	AST (IU/l)	ALT (IU/l)	ALP (IU/l)	BUN (mg/dl)	Cre (mg/dl)
24 hours after injection						
PBS	2.8 ± 0.09	68.8 ± 7.3	27.6 ± 4.6	202 ± 22.0	25.6 ± 2.7	0.14 ± 0.01
AAV9-shSOD1	2.9 ± 0.1	78.0 ± 15.9	40.3 ± 9.8	193 ± 50.0	26.4 ± 1.9	0.13 ± 0.01
AAV9-shTRPV1	3.0 ± 0.1	71.0 ± 2.9	30.2 ± 3.1	214 ± 18.4	25.9 ± 1.9	0.13 ± 0.01
16 weeks after injection						
PBS	2.4 ± 0.03	87.3 ± 25.2	27.3 ± 6.0	203 ± 41.0	27.5 ± 1.7	0.19 ± 0.02
AAV9-shSOD1	2.3 ± 0.1	79.7 ± 17.7	37.3 ± 10.4	225 ± 19.4	23.6 ± 2.4	0.22 ± 0.02
AAV9-shTRPV1	2.6 ± 0.3	69.3 ± 2.6	31.3 ± 3.5	225 ± 26.4	25.1 ± 0.7	0.18 ± 0.01

The values shown are mean values ± SEM (n = 3).
Abbreviations: AST, aspartate aminotransferase; ALT, alanine aminotransferase; ALP, alkaline phosphatase; BUN, blood urea nitrogen; PBS, phosphate-buffered saline.

growth factor, neurotrophin-3, or brain-derived neurotrophic factor), inflammatory cytokines (*e.g.*, tumor necrosis factor, interferon, or interleukin), ion channels (*e.g.*, voltage-gated sodium channels and calcium channels), and neurotransmitters (*e.g.*, calcitonin gene-related peptide or substance P), which may prove to be more attractive therapeutic targets than TRPV1 in the treatment of neuropathic pain. The present study thus demonstrates the power of intrathecal AAV-mediated gene transfer as an investigative and potentially therapeutic tool in the nervous system.

MATERIALS AND METHODS

Plasmid construct. The TRPV1 coding sequence was subcloned in-frame from a TRPV1 plasmid, which was a kind gift from Dr. Michael Xi Zhu, into the HinDIII-XbaI sites of the pBluescriptII KS (+) vector (Stratagene, La Jolla, CA). The pBluescriptII KS (+)-TRPV1 product was then subcloned in-frame into the XhoI sites of psiCHECK-2 (Promega, Madison, WC). We confirmed based on quantitative PCR and a luciferase assay that HEK293T cells stably expressed both dual luciferase and TRPV1 after transfection of the psiCHECK-2 TRPV1 plasmid (**Figure 1c**).

Cell culture and dual luciferase assay for selecting the shRNA sequence. HEK293T cells were transfected with both the psiCHECK-2 vector encoding TRPV1 and each siRNA sequence using Lipofectamine Plus reagent (Life Technologies, Rockville, MD) in Opti-MEM (Invitrogen, Carlsbad, CA). After 48 hours, cells were maintained in D-MEM (Invitrogen) supplemented with 10% fetal bovine serum (Invitrogen), penicillin (100 units/ml) and streptomycin (100 µg/ml; Invitrogen). Seven siRNA sequences targeting TRPV1 were designed: siRNA-1 (nucleotide 604–624), siRNA-2 (nucleotide 1,229–1,249), siRNA-3 (nucleotide 1,295–1,315), siRNA-5 (nucleotide 1,727–1,747), siRNA-6 (nucleotide 1,734–1,754), siRNA-7 (nucleotide 1,868–1,888) were newly designed. siRNA-4 was previously published.[30] Cells were washed two times in PBS and harvested using Passive Lysis Buffer (Promega), followed by freezing at −80 °C for 15 minutes. The lysate was processed to measure *firefly* and *renilla* luciferase activity, and relative luminescence units were determined using a luminometer (GL-200: Standard type, Microtec, Chiba, Japan) and Dual-Luciferase Reporter Assay System (Promega) according to the manufacturer's instructions. Among the seven candidate siRNAs, the sequence showing the highest suppression of *renilla* luciferase activity (siRNA-6) was selected. Subsequently, referring to the construct of siRNA-6, two shRNA sequences were designed (**Figure 1b**) and investigated based on luciferase assay in order to select for the shRNA to be expressed from AAV9 vector. We also investigated which shRNA is most silencing efficiency.

Construction, production, and titration of AAV9-shTRPV1. The shRNA-A cassette and anti-SOD1 shRNA cassette as a negative control sequence were prepared as previously described.[12,47] Each shRNA cassette was cloned downstream of the human polymerase III U6 promoter in the AAV9 vector plasmid (Stratagene). The recombinant AAV9 vector was produced and purified as previously reported (**Figure 1e**).[12] HEK293 cells at ~70% confluence were transfected with the AAV9 packaging plasmid pRep2/Cap9 (gift from Dr. James M Wilson, University of Pennsylvania, Philadelphia, PA) and adenovirus helper plasmid (Stratagene) at a ratio of 1:1:1. At 6 hours after transfection, the culture medium was replaced with fresh medium, and the cells were incubated for 48 hours. The cells were then harvested from the culture dishes and pelleted by centrifugation, resuspended in PBS, and subjected to three rounds of freeze thawing. Cell debris was then pelleted by centrifugation at 1,200*g* for 15 minutes. AAV vectors were purified using ammonium sulfate precipitation and iodixanol (Axis-Shield) continuous gradient centrifugation. Size-exclusion chromatography was performed using an AKTA Explorer 100 HPLC system (GE Healthcare, Japan Corporation, Tokyo, Japan) equipped with a 2-mL sample loop. A Superdex 200 10/300 GL column (GE Healthcare) was equilibrated with minor histocompatibility antigen buffer (3.3 mmol/l Mes, 3.3 mmol/l Hepes, 3.3 mM NaOAc, 50 mmol/l NaCl, pH 6.5). The vector-containing fractions were loaded onto the column at a flow rate of 0.5 ml/minute, and the eluate was collected as 0.5 ml fractions over the duration of one column volume (23 ml). AAV peak fractions were identified by 280/260 nm absorbance and real-time quantitative polymerase chain reaction using vector-specific primers. The purified AAVs were then concentrated further by using Amico Ultra-4 tubes (Ultracel-30k; Merck Millipore Japan, Tokyo, Japan) to a final concentration of 2×10^{12} genome copies/ml, as determined by quantitative polymerase chain reaction. The genome copy number was calculated by TaqMan PCR (Applied Biosystems, Foster City, CA). The vectors were treated with Benzonase and digested with proteinase K (Wako Pure Chemical Industries, Osaka, Japan) for 1 hour and purified by phenol-chloroform extraction. The TaqMan primers and probe were designed as follows: forward primer: 5′-CAGGCTGGTCCAACTCCTA-3′, reverse primer: 5′-GCAGTGGTTCACGCCTGTAA-3′, and probe: 5′-TACCCACCTTGGCCTC-3′. The designed TaqMan PCR fragment was located in the human growth hormone poly A site in the vector.

Animals. Eight-week-old female Institute of Cancer Research mice weighing 25–35 g were used. Animals were kept under standard laboratory conditions with free access to standard laboratory food and tap water. The body weight of the mice was measured every week. All animal experiments were performed in accordance with the Ethical and Safety Guidelines for Animal Experiments of Tokyo Medical and Dental University and approved by the Animal Experiment Committee of Tokyo Medical and Dental University (#81213).

Animal model of neuropathic pain. Mice underwent surgery involving ligation of the tibial and common peroneal nerve according to the SNI model.[13] Animals were anesthetized by intraperitoneal injection of chloral hydrate (0.5 mg per g body weight). The surgical site (left leg) was shaved and disinfected. An incision was made on the lateral mid-thigh, and the

underlying muscles were separated to expose the sciatic nerve. The common peroneal and tibial nerves were then tight-ligated with 8.0 silk and sectioned distal to the ligation to remove 2–4 mm of the distal nerve stump (**Figure 2a**). Great care was taken to avoid any contact with or stretching of the intact sural nerve. The muscles and skin were closed in two layers using 4.0 monofilament nylon sutures. After the operation, animals were allowed to recover in their own cages.

Intrathecal treatment after SNI. Three weeks after nerve injury, when obvious behavioral hypersensitivity was observed, all mice were given intrathecal injections of AAV9-shTRPV1, AAV9-shSOD1, or PBS. After induction of anesthesia using intraperitoneal injections of chloral hydrate (0.5 mg per g body weight) and ketamine hydrochloride (0.05 mg per g body weight), each animal was shaved and disinfected. The mice were placed in the prone position, and a partial laminectomy of the caudal portion of the second lumbar vertebra and the rostral portion of the third lumbar vertebra were performed. The dura mater was exposed and punctured using a 27-gauge needle. Subsequently, a 10-mm PE-10 catheter was connected to a 10-μl Hamilton syringe, Hamilton Company (Watertown, MA) and inserted caudally into the subarachnoid space between the second and third lumbar vertebrae (**Figure 3a**). The tip of the catheter was located approximately at the level of L4. A volume of 10 μl (2×10^{12} vector genomes per microliter) of AAV9-shTRPV1, AAV9-shSOD1, or PBS was injected slowly over a 2-minute period. After the catheter was removed, the incision was sutured, and the mice were maintained in the head-up position and allowed to recover on a heating pad. Four weeks after the injection, all of the mice were euthanized, and the lumbar spinal cord and ipsilateral L5 and L6 DRGs were harvested for analysis.

AAV vector genomic DNA PCR. The spinal cord was obtained in separate segments from C6 to C8, T2 to T4, T10 to T12, and L1 to L3. The DRGs were also collected from bilateral C6 to C8, bilateral T2 to T4, bilateral T10 to T12, and bilateral L1 to L3. Whole genomic DNA was extracted from the harvested tissues. Vector genomic DNA was amplified using primers and probes targeting the human growth hormone cassette and yielding a 84-bp fragment. Forward 5′-CAGGCTGGTCCAACTCCTA-3′, reverse 5′-GCAGTGGTTCACGCCTGTAA-3′ served as the primer set, and 5′-TACCCACCTTGGCCTC-3′ served as the probe.

Measurement of mRNA expression by quantitative RT-PCR. Total RNA was extracted from the harvested tissues, including the lumbar DRG and the lumbar segment of the spinal cord, using Isogen (Nippon Gene, Tokyo, Japan). The RNA samples obtained from the lumbar spinal cord were collected from the lumbar region located at the first to second vertebral level. The RNA samples obtained from the DRG were obtained from the L5 and L6 DRG. DNase I-treated total RNA (0.5 μg) was reverse transcribed using SuperScript III Reverse Transcriptase (Invitrogen). The cDNA was amplified using the quantitative TaqMan system on a Light Cycle 480 Real-Time PCR Instrument (Roche, Basel, Switzerland), according to the manufacturer's protocol. As an internal control, *gapdh* cDNA was also quantitatively amplified using a TaqMan primer and probe set (Applied Biosystems). Primer and probe sets for mouse *trpv1* and mouse *ifnβ* were also designed by Applied Biosystems. The ratio of *trpv1* mRNA expression to *gapdh* mRNA expression was calculated to estimate the shRNA silencing efficiency.

Western blotting. The lumbar spinal cord located between the first and second vertebrae and ipsilateral L5 and L6 DRGs were isolated carefully from treated mice. The tissues were homogenized in cold homogenization buffer containing 0.1% sodium dodecylsulfate, 1% sodium deoxycholate, 1% Triton X-100, and 1 mmol/l phenylmethylsulfonyl fluoride together with a protein inhibitor cocktail (Roche, Penzberg, Germany). Five micrograms of extracted protein from each sample were mixed with Laemmli sample buffer (BioRad, Hercules, CA), denatured at 37 °C for 60 minutes, and separated on a 15% sodium dodecylsulfate–polyacrylamide gel electrophoresis. The separated proteins were transferred to a polyvinylidene difluoride membrane (BioRad) and then incubated with specific primary antibodies, including a rabbit anti-TRPV1 antibody (1:1,000; Transgenic, Kumamoto, Japan) and a mouse anti-glyceraldehyde-3-phosphate dehydrogenase monoclonal antibody (Biodesign, Saco, ME). After incubation, the membranes were rinsed and incubated with a 0.1% solution of horseradish peroxidase-conjugated secondary antibodies, including goat anti-rabbit HRP IgG and goat anti-mouse HRP IgG (Thermo Science, Rockford, IL). The protein–antibody interactions were visualized using the SuperSignal West Femto Maximum Sensitivity Substrate (Thermo Science).

Immunohistochemistry. Mice were sacrificed at 24 hours after single or repeated injection of AAV9-shTRPV1, AAV9-shSOD1, or PBS by transcardiac perfusion of PBS for 5 minutes at room temperature, followed by 4% paraformaldehyde in PBS for 15 minutes at 4 °C. After perfusion, the lumbar spinal cord and DRG were immediately removed and postfixed in 4% paraformaldehyde in PBS at 4 °C overnight. After postfixation, the samples were transferred to PBS containing 30% sucrose and dehydrated for 3 days. The tissues were then embedded in low melting temperature agarose (BM Equipment, Tokyo, Japan) in PBS. Frozen sections ~20 μm thick were sectioned from the L5 DRG and the spinal cord at the first lumbar vertebral level from mice in each group and then incubated for 30 minutes at room temperature in a blocking solution (5% normal goat serum). The sections were then incubated with a rabbit polyclonal anti-CD8 antibody (1:500, Abcam, Tokyo, Japan) for 24 hours at 4 °C. Following incubation, the sections were washed and incubated for 30 minutes at room temperature with a biotinylated secondary antibody (1:200, Vector Laboratories, Ontario, Canada) in 0.5% horse serum. The sections were then incubated with ABC reagent (Vector Laboratories) for 30 minutes, followed by incubation with a peroxidase substrate solution for 2 minutes. After washing, the tissue sections were counter stained with hematoxylin for 1 minute.

Sensory behavioral tests. Animals were placed in Plexiglas boxes with dimensions of $9.5 \times 21 \times 25$ cm and allowed to acclimate to the testing environment. The boxes were then placed on an elevated perforated plastic surface for a minimum of 30 minutes prior to all behavioral tests.[48] Two observers who were blind to the experimental group assignments performed the behavioral testing once a week and at specific time points for 16 weeks in total.

Tactile threshold. Mechanical sensitivity was measured by applying a series of calibrated von Frey filaments (0.02–8 g) to the plantar aspect of the hindpaw. Each filament was applied once to each mouse. Beginning with the 1-g filament, each filament was applied perpendicular to the hind paw for 4–6 seconds. A brisk withdrawal of the hind paw indicated a positive response, and a lack of withdrawal indicated a negative response. The filament testing was repeated two times, and at least two responses to the filament out of the three trials indicated an overall positive response. If the mouse demonstrated an overall positive response, the filament with the next lower force was applied as described above. If no overall positive response was observed (0/3 or 1/3 responses), the filament with the next higher force was applied as described above. Once the threshold was determined (*i.e.*, from response to no response, or vice versa) the responses to the next five filaments were recorded to determine the median withdrawal threshold.

Response to acetone. Using a plastic tube connected to a 1-ml syringe, and without touching the skin, 100 μl of acetone were applied to the plantar surface of the hindpaw. Acetone was applied five times to each paw at an interval of at least 30 seconds, and the number of brisk foot withdrawals in response to the acetone application was recorded.

Response to noxious heat stimulus. Responses to noxious heat were determined using a hot plate (NISSIN, Saitama, Japan). The mice were placed in a transparent plastic chamber on a 50 or 55 °C metal hot plate to measure the latency of paw flinching, licking or withdrawal. A maximum cutoff of 30 seconds was used to prevent tissue damage. A 5-minute interval

between consecutive stimulations of the same hind paw was employed. Testing was performed three times on left lateral plantar hindpaw, and the withdrawal latencies were averaged. In addition, we defined analgesia as a change in the latency of withdrawal from the 50 °C hot plate after injection of AAV9-shTRPV1, relative to the preinjection latency.

Statistical analyses. All data are presented as the mean ± standard error of the mean (n = 3–9). We performed the statistical analysis using two-way analysis of variance with repeated measures for comparisons among the three groups for all experiments. In case of a significant treatment effect, pairwise comparisons were performed in a *post hoc* analysis with Bonferroni adjustment. The group size was n = 6–12. Significance was defined as $P < 0.05$.

ACKNOWLEDGMENTS

We thank Michael Xi Zhu (Department of Integrative Biology and Pharmacology, The University of Texas Health Science Center at Houston Medical School) for kindly providing the TRPV1 plasmid and Miho Sekiguchi (Department of Orthopedic Surgery, Fukushima Medical University School of Medicine) and Igor Spigelman (Division of Oral Biology & Medicine, School of Dentistry, The University of California, Los Angeles) for technical support. This work was supported in part by a Grant-in-aid for Scientific Research (C) from the Japan Society for the Promotion of Science and a Grant-in-aid from the General Insurance Association of Japan.

REFERENCES

1. Campbell, JN and Meyer, RA (2006). Mechanisms of neuropathic pain. *Neuron* **52**: 77–92.
2. Finnegan, TF, Chen, SR and Pan, HL (2005). Effect of the {mu} opioid on excitatory and inhibitory synaptic inputs to periaqueductal gray-projecting neurons in the amygdala. *J Pharmacol Exp Ther* **312**: 441–448.
3. Wilson, SP, Yeomans, DC, Bender, MA, Lu, Y, Goins, WF and Glorioso, JC (1999). Antihyperalgesic effects of infection with a preproenkephalin-encoding herpes virus. *Proc Natl Acad Sci USA* **96**: 3211–3216.
4. Meunier, A, Latrémolière, A, Mauborgne, A, Bourgoin, S, Kayser, V, Cesselin, F *et al.* (2005). Attenuation of pain-related behavior in a rat model of trigeminal neuropathic pain by viral-driven enkephalin overproduction in trigeminal ganglion neurons. *Mol Ther* **11**: 608–616.
5. Clapham, DE (2003). TRP channels as cellular sensors. *Nature* **426**: 517–524.
6. Levine, JD and Alessandri-Haber, N (2007). TRP channels: targets for the relief of pain. *Biochim Biophys Acta* **1772**: 989–1003.
7. Pogatzki-Zahn, EM, Shimizu, I, Caterina, M and Raja, SN (2005). Heat hyperalgesia after incision requires TRPV1 and is distinct from pure inflammatory pain. *Pain* **115**: 296–307.
8. Yokota, T, Iijima, S, Kubodera, T, Ishii, K, Katakai, Y, Ageyama, N *et al.* (2007). Efficient regulation of viral replication by siRNA in a non-human primate surrogate model for hepatitis C. *Biochem Biophys Res Commun* **361**: 294–300.
9. Baigude, H, McCarroll, J, Yang, CS, Swain, PM and Rana, TM (2007). Design and creation of new nanomaterials for therapeutic RNAi. *ACS Chem Biol* **2**: 237–241.
10. Nishina, K, Unno, T, Uno, Y, Kubodera, T, Kanouchi, T, Mizusawa, H *et al.* (2008). Efficient *in vivo* delivery of siRNA to the liver by conjugation of alpha-tocopherol. *Mol Ther* **16**: 734–740.
11. Rodriguez-Lebron, E, Denovan-Wright, EM, Nash, K, Lewin, AS and Mandel, RJ (2005). Intrastriatal rAAV-mediated delivery of anti-huntingtin shRNAs induces partial reversal of disease progression in R6/1 Huntington's disease transgenic mice. *Mol Ther* **12**: 618–633.
12. Hirai, T, Enomoto, M, Machida, A, Yamamoto, M, Kuwahara, H, Tajiri, M *et al.* (2012). Intrathecal shRNA-AAV9 inhibits target protein expression in the spinal cord and dorsal root ganglia of adult mice. *Hum Gene Ther Methods* **23**: 119–127.
13. Decosterd, I and Woolf, CJ (2000). Spared nerve injury: an animal model of persistent peripheral neuropathic pain. *Pain* **87**: 149–158.
14. Calixto, JB, Kassuya, CA, André, E and Ferreira, J (2005). Contribution of natural products to the discovery of the transient receptor potential (TRP) channels family and their functions. *Pharmacol Ther* **106**: 179–208.
15. Chan, CL, Facer, P, Davis, JB, Smith, GD, Egerton, J, Bountra, C *et al.* (2003). Sensory fibres expressing capsaicin receptor TRPV1 in patients with rectal hypersensitivity and faecal urgency. *Lancet* **361**: 385–391.
16. Schäfers, M, Geis, C, Svensson, CI, Luo, ZD and Sommer, C (2003). Selective increase of tumour necrosis factor-alpha in injured and spared myelinated primary afferents after chronic constrictive injury of rat sciatic nerve. *Eur J Neurosci* **17**: 791–804.
17. Hudson, LJ, Bevan, S, Wotherspoon, G, Gentry, C, Fox, A and Winter, J (2001). VR1 protein expression increases in undamaged DRG neurons after partial nerve injury. *Eur J Neurosci* **13**: 2105–2114.
18. Rasband, MN, Park, EW, Vanderah, TW, Lai, J, Porreca, F and Trimmer, JS (2001). Distinct potassium channels on pain-sensing neurons. *Proc Natl Acad Sci USA* **98**: 13373–13378.
19. Fukuoka, T, Tokunaga, A, Tachibana, T, Dai, Y, Yamanaka, H and Noguchi, K (2002). VR1, but not P2X(3), increases in the spared L4 DRG in rats with L5 spinal nerve ligation. *Pain* **99**: 111–120.
20. Facer, P, Casula, MA, Smith, GD, Benham, CD, Chessell, IP, Bountra, C *et al.* (2007). Differential expression of the capsaicin receptor TRPV1 and related novel receptors TRPV3, TRPV4 and TRPM8 in normal human tissues and changes in traumatic and diabetic neuropathy. *BMC Neurol* **7**: 11.
21. Obata, K, Katsura, H, Sakurai, J, Kobayashi, K, Yamanaka, H, Dai, Y *et al.* (2006). Suppression of the p75 neurotrophin receptor in uninjured sensory neurons reduces neuropathic pain after nerve injury. *J Neurosci* **26**: 11974–11986.
22. Hwang, SJ, Burette, A, Rustioni, A and Valtschanoff, JG (2004). Vanilloid receptor VR1-positive primary afferents are glutamatergic and contact spinal neurons that co-express neurokinin receptor NK1 and glutamate receptors. *J Neurocytol* **33**: 321–329.
23. Kosugi, M, Nakatsuka, T, Fujita, T, Kuroda, Y and Kumamoto, E (2007). Activation of TRPA1 channel facilitates excitatory synaptic transmission in substantia gelatinosa neurons of the adult rat spinal cord. *J Neurosci* **27**: 4443–4451.
24. Ferrini, F, Salio, C, Vergnano, AM and Merighi, A (2007). Vanilloid receptor-1 (TRPV1)-dependent activation of inhibitory neurotransmission in spinal substantia gelatinosa neurons of mouse. *Pain* **129**: 195–209.
25. Kim, YH, Back, SK, Davies, AJ, Jeong, H, Jo, HJ, Chung, G *et al.* (2012). TRPV1 in GABAergic interneurons mediates neuropathic mechanical allodynia and disinhibition of the nociceptive circuitry in the spinal cord. *Neuron* **74**: 640–647.
26. Ossipov, MH, Bian, D, Malan, TP Jr, Lai, J and Porreca, F (1999). Lack of involvement of capsaicin-sensitive primary afferents in nerve-ligation injury induced tactile allodynia in rats. *Pain* **79**: 127–133.
27. Caterina, MJ, Leffler, A, Malmberg, AB, Martin, WJ, Trafton, J, Petersen-Zeitz, KR *et al.* (2000). Impaired nociception and pain sensation in mice lacking the capsaicin receptor. *Science* **288**: 306–313.
28. Culshaw, AJ, Bevan, S, Christiansen, M, Copp, P, Davis, A, Davis, C *et al.* (2006). Identification and biological characterization of 6-aryl-7-isopropylquinazolinones as novel TRPV1 antagonists that are effective in models of chronic pain. *J Med Chem* **49**: 471–474.
29. Christoph, T, Grünweller, A, Mika, J, Schäfer, MK, Wade, EJ, Weihe, E *et al.* (2006). Silencing of vanilloid receptor TRPV1 by RNAi reduces neuropathic and visceral pain in vivo. *Biochem Biophys Res Commun* **350**: 238–243.
30. Klusáková, I and Dubový, P (2009). Experimental models of peripheral neuropathic pain based on traumatic nerve injuries - an anatomical perspective. *Ann Anat* **191**: 248–259.
31. Davis, JB, Gray, J, Gunthorpe, MJ, Hatcher, JP, Davey, PT, Overend, P *et al.* (2000). Vanilloid receptor-1 is essential for inflammatory thermal hyperalgesia. *Nature* **405**: 183–187.
32. Jordt, SE, McKemy, DD and Julius, D (2003). Lessons from peppers and peppermint: the molecular logic of thermosensation. *Curr Opin Neurobiol* **13**: 487–492.
33. Patapoutian, A, Peier, AM, Story, GM and Viswanath, V (2003). ThermoTRP channels and beyond: mechanisms of temperature sensation. *Nat Rev Neurosci* **4**: 529–539.
34. Moran, MM, Xu, H and Clapham, DE (2004). TRP ion channels in the nervous system. *Curr Opin Neurobiol* **14**: 362–369.
35. Tominaga, M and Caterina, MJ (2004). Thermosensation and pain. *J Neurobiol* **61**: 3–12.
36. Vriens, J, Owsianik, G, Hofmann, T, Philipp, SE, Stab, J, Chen, X *et al.* (2011). TRPM3 is a nociceptor channel involved in the detection of noxious heat. *Neuron* **70**: 482–494.
37. Cho, H, Yang, YD, Lee, J, Lee, B, Kim, T, Jang, Y *et al.* (2012). The calcium-activated chloride channel anoctamin 1 acts as a heat sensor in nociceptive neurons. *Nat Neurosci* **15**: 1015–1021.
38. Shimosato, G, Amaya, F, Ueda, M, Tanaka, Y, Decosterd, I and Tanaka, M (2005). Peripheral inflammation induces up-regulation of TRPV2 expression in rat DRG. *Pain* **119**: 225–232.
39. Park, U, Vastani, N, Guan, Y, Raja, SN, Koltzenburg, M and Caterina, MJ (2011). TRP vanilloid 2 knock-out mice are susceptible to perinatal lethality but display normal thermal and mechanical nociception. *J Neurosci* **31**: 11425–11436.
40. Moqrich, A, Hwang, SW, Earley, TJ, Petrus, MJ, Murray, AN, Spencer, KS *et al.* (2005). Impaired thermosensation in mice lacking TRPV3, a heat and camphor sensor in the skin. *Science* **307**: 1468–1472.
41. Suhy, DA, Kao, SC, Mao, T, Whiteley, L, Denise, H, Souberbielle, B *et al.* (2012). Safe, long-term hepatic expression of anti-HCV shRNA in a nonhuman primate model. *Mol Ther* **20**: 1737–1749.
42. Janson, C, McPhee, S, Bilaniuk, L, Haselgrove, J, Testaiuti, M, Freese, A *et al.* (2002). Clinical protocol. Gene therapy of Canavan disease: AAV-2 vector for neurosurgical delivery of aspartoacylase gene (ASPA) to the human brain. *Hum Gene Ther* **13**: 1391–1412.
43. Kaplitt, MG, Feigin, A, Tang, C, Fitzsimons, HL, Mattis, P, Lawlor, PA *et al.* (2007). Safety and tolerability of gene therapy with an adeno-associated virus (AAV) borne GAD gene for Parkinson's disease: an open label, phase I trial. *Lancet* **369**: 2097–2105.
44. Boutin, S, Monteilhet, V, Veron, P, Leborgne, C, Benveniste, O, Montus, MF *et al.* (2010). Prevalence of serum IgG and neutralizing factors against adeno-associated virus (AAV) types 1, 2, 5, 6, 8, and 9 in the healthy population: implications for gene therapy using AAV vectors. *Hum Gene Ther* **21**: 704–712.
45. Bartel, M, Schaffer, D and Büning, H (2011). Enhancing the Clinical Potential of AAV Vectors by Capsid Engineering to Evade Pre-Existing Immunity. *Front Microbiol* **2**: 204.
46. Kappel, S, Matthess, Y, Kaufmann, M and Strebhardt, K (2007). Silencing of mammalian genes by tetracycline-inducible shRNA expression. *Nat Protoc* **2**: 3257–3269.
47. Yokota, T, Miyagishi, M, Hino, T, Matsumura, R, Tasinato, A, Urushitani, M *et al.* (2004). siRNA-based inhibition specific for mutant SOD1 with single nucleotide alternation in familial ALS, compared with ribozyme and DNA enzyme. *Biochem Biophys Res Commun* **314**: 283–291.
48. Hargreaves, K, Dubner, R, Brown, F, Flores, C and Joris, J (1988). A new and sensitive method for measuring thermal nociception in cutaneous hyperalgesia. *Pain* **32**: 77–88.

Spine

SPINE Volume 39, Number 2, pp 113-119

CERVICAL SPINE

Dynamic Changes in Spinal Cord Compression by Cervical Ossification of the Posterior Longitudinal Ligament Evaluated by Kinematic Computed Tomography Myelography

Toshitaka Yoshii, MD, PhD,*† Tsuyoshi Yamada, MD,*† Takashi Hirai, MD, PhD,*† Takashi Taniyama, MD,*† Tsuyoshi Kato, MD, PhD,* Mitsuhiro Enomoto, MD, PhD,*† Hiroyuki Inose, MD, PhD,*† Satoshi Sumiya, MD,* Shigenori Kawabata, MD, PhD,* Kenichi Shinomiya, MD, PhD,*†‡ and Atsushi Okawa, MD, PhD*†‡

Study Design. A prospective clinical study.

Objective. To investigate the dynamic causative factor in the pathogenesis of myelopathy in patients with cervical ossification of the posterior longitudinal ligament (OPLL) using kinematic computed tomography (CT) myelography.

Summary of Background Data. Kinematic CT myelography is useful for dynamically evaluating the cervical spine with high-resolution images, particularly in bony compressive lesions. However, no studies have evaluated the dynamic factors in patients with OPLL using kinematic CT myelography.

Methods. From 2008 to 2013, 51 consecutive patients with OPLL who presented with myelopathy were prospectively enrolled in this study. The patients were examined with kinematic (flexion-extension) CT myelography using a multidetector CT scanner. The range of motion at C2–C7 from flexion to extension was measured in the sagittal view. The segmental range of motion, anterior-posterior diameter and cross-sectional area (CSA) of the spinal cord were measured at the level where the spinal cord was most compressed by OPLL.

Results. The neurological condition of the patients evaluated by Japanese Orthopaedic Association scores were 10.8 ± 2.4 points. The mean range of motion at C2–C7 and at the most compressed segment were 23.1 ± 11.7 and 7.0 ± 4.4°, respectively. Both the anterior-posterior diameter and the CSA at the most compressed levels were significantly decreased during neck extension compared with flexion. Interestingly, the anterior-posterior diameter and the CSA were decreased during neck flexion in 13.7% (7/51) of the patients. All 7 of these patients had massive OPLL with an occupying rate 60% or more. The dynamic change rate of CSA (flexion/extension) was significantly smaller in patients with an OPLL occupying rate 60% or more compared with patients with an occupying rate less than 60%.

Conclusion. Although spinal cord compression was increased during neck extension in most of the patients, greater levels of compression could be placed on the spinal cord during neck flexion when the patients had OPLL with a high occupying rate.

Key words: ossification of the posterior longitudinal ligament, computed tomography myelography, kinematic study, compressive myelopathy.

Level of Evidence: 4

Spine 2014;39:113–119

Cervical spondylosis and ossification of the posterior longitudinal ligament (OPLL) are common degenerative spine diseases that cause progressive neurological dysfunction in middle-aged and elderly patients.[1,2] Static factors, such as congenital canal narrowing, degenerative intervertebral discs, osteophyte formation, and thickening of ligamentum flavum, are important in the pathogenesis of cervical myelopathy. However, dynamic factors induced by cervical spinal motion, such as anterior or posterior translation of vertebrae, disc protrusion, and buckling of the flavum,[3] are known to contribute to the development and progression of neurological symptoms in cervical spondylotic myelopathy (CSM)[4,5] and cervical OPLL.[6–8] Various radiological examinations, including plain radiograph, computed tomography (CT), and magnetic resonance imaging (MRI), have been performed to evaluate the static structural abnormality of the

From the *Section of Orthopaedic and Spinal Surgery, Graduate School and †Section of Regenerative Therapeutics for Spine and Spinal Cord, Graduate School, Tokyo Medical and Dental University, Bunkyo-ku, Tokyo, Japan; and ‡Global Center of Excellence (GCOE) Program for International Research Center for Molecular Science in Tooth and Bone Disease, Tokyo Medical and Dental University, Kanda-Surugadai, Chiyoda-ku, Tokyo, Japan.

Acknowledgment date: August 2, 2013. First revision date: September 21, 2013. Acceptance date: October 12, 2013.

The device(s)/drug(s) is/are FDA-approved or approved by corresponding national agency for this indication.

No funds were received in support of this work.

Relevant financial activities outside the submitted work: grants/grants pending.

Address correspondence and reprint requests to Toshitaka Yoshii, MD, PhD, Department of Orthopaedic and Spinal Surgery, Graduate School, Tokyo Medical and Dental University, 1-5-45 Yushima, Bunkyo-ku, Tokyo, 113-8519, Japan; E-mail: yoshii.orth@tmd.ac.jp

DOI: 10.1097/BRS.0000000000000086